Vitamin D promotes DNase1L3 to degrade ecDNA and inhibit the malignant progression of hepatocellular carcinoma

Heng Zhang[1,2]†, Lu-ning Qin[1]†, Qing-qing Li[1], Ting Wu[1], Lei Zhang[1], Kai-wen Wang[1,2], Shan-bin Cheng[1,2], Yue Shi[1], Yi-qian Feng[1], Jing-xia Han[1,2], Yi-nan Li[1], Zhi-yang Li[1], Hui-juan Liu[1,2], Tao Sun[1]*

[1]State Key Laboratory of Medicinal Chemical Biology and College of Pharmacy, Nankai University, Tianjin, China

[2]Tianjin International Joint Academy of Biomedicine, Tianjin, China

†These authors contributed equally to this work.

*Corresponding author: Tao Sun, **email:** tao.sun@nankai.edu.cn

Abstract

Extrachromosomal DNA (ecDNA) is an important carrier of oncogene amplification. However, the degradation mechanism of ecDNA is not well understood. We found that endogenous natural molecular vitamin D (VD) reduces ecDNA and inhibits the progression of hepatocellular carcinoma. VD reduces ecDNA depending on its binding protein GC, which can interact with the endonuclease DNase1L3 and stabilize DNase1L3 protein level. The DNase1L3 protein directly degrades ecDNA, and its N-terminus has a lipophilic region capable of affinity for lipid droplets. Intranuclear lipid droplets are abundantly distributed around ecDNA, so DNase1L3 can affinitize ecDNA through its lipophilic region. VD, as a lipid-soluble molecule, can increase the area of lipid droplets and further improve the degradation of DNase1L3 on ecDNA. Therefore, we designed two mRNA-based therapeutics, DNase1L3 and GC-DNase, both of which had an anti-tumor effect on PDX models. The above results showed that treatments targeting ecDNA in cancer are prospective in clinical practice.

One-Sentence Summary

Vitamin D reduces ecDNA and inhibits cancer progression. DNase1L3 was found to degrade ecDNA with the help of lipid droplets.

Introduction

The DNA of the vast majority of eukaryotic cells is located on the chromatin (chromosome) of the nucleus. However, as early as the 20th century, scientists discovered that DNA is also present outside of chromatin, such as mitochondrial DNA, plasmids in yeast, and double minutes in cancer cells (*1*). The DNA outside of chromatin is circular and named extrachromosomal circular DNA, but its formation and function have only been studied in detail in recent years. In 2017, Paul S. Mischel et al. found that a large number of oncogenes in cancer cells are amplified in the form of ecDNA, which are large enough to carry intact genes, also known as ecDNA(*2*). In 2019, researchers further proved that ecDNA in cancer displays significantly enhanced chromatin accessibility and high transcription levels(*3*, *4*). In 2020, the research group used pan-cancer whole genome sequencing data for in-depth analysis and found that ecDNA amplification frequently occurs in most cancer types, and patients whose cancers carried ecDNA had significantly shorter survival(*5*). Thus, ecDNA has important clinical significance.

However, the balancing mechanism by which cells respond to ecDNA, i.e., how ecDNA degrades within cells, is unclear. On the basis of the obvious clinical significance of ecDNA, whether ecDNA can become a target for anti-cancer drugs should be studied. If so, the drugs that can target ecDNA are currently unknown. It was believed that the unique features of ecDNA provide at least five potential strategies for therapy (*6*), but no one have been developed. We found that vitamin D (VD) can reduce ecDNA levels in hepatocellular carcinoma (HCC) cells, and further research found that DNase1L3 can directly degrade ecDNA.

VD is an inexpensive and readily available pharmacologically active molecule that, in addition to playing a role in bone metabolism and calcium homeostasis, has a role in cancer treatment, especially in breast, prostate, and colon cancers (*7*). Clinical studies have confirmed that the higher serum concentration of VD, the lower the risk of cancer (*8*). Moreover, it has been reported that VD supplementation can reduce the incidence of cancer (*9*). In addition to this, in 2019, the results of a clinical META analysis of 6,537 patients showed that VD supplementation reduced cancer mortality (*10*). In terms of HCC, high serum concentration of VD is associated with prolonged survival in HCC (*11*). Cellular and animal experiments have confirmed that VD also inhibits breast and prostate cancer, as well as leukemia and lymphoma. However, the molecular mechanism of VD antitumor activity is unclear.

This work studied the anti-tumor effect of VD and the degradation of ecDNA, revealed the pharmacological role of VD from a new perspective, and provided ideas for drug development targeting ecDNA. The study found that DNase1L3 could degrade ecDNA, possessed the properties of tumor suppressor genes, and exhibited the potential to develop biological drugs that degrade ecDNA. The study also designed two mRNA drugs, DNase1L3 and GC-DNase, to evaluate the potential clinical effects using PDX models.

Results

VD reduces ecDNA level in HCC cells

To screen for pharmacologically active molecules capable of decreasing the ecDNA level, we selected common pharmacologically active molecules that have antitumor effects for metaphase chromosome spread assay and quantified by image analysis with the ecSeg algorithm(*12*). These pharmacologically active molecules included 25-hydroxy vitamin D3 (25OHD, the main form of VD in peripheral blood), vitamin C, sodium butyrate, metformin, and natural molecules such as artemisinin, puerarin, and baicalein. We found that nine molecules showed varying degrees of reduction in ecDNA quantity after treatment, with 25OHD having the most pronounced effect (Fig. S1, A and B). Therefore, we started our study with the pharmacological effects of VD. We selected different forms of VD including Vitamin D3 (VD3), 25-hydroxy vitamin D3 (25OHD), and 1,25-dihydroxyvitamin D (1,25$(OH)_2$D) to evaluate the specific effect of the active isomer of VD on decreasing the ecDNA levels, as shown in Fig. S1, C and D, VD3 and 25OHD had an effect on decreasing the ecDNA levels, while 1,25$(OH)_2$D revealed almost no effect. So, we conducted a follow-up cell experiments with 25OHD in this study. 1,25$(OH)_2$D, which is considered to be one of the active forms of VD, had almost no effect on decreasing the ecDNA levels, which was unexpected, it was consequently used as an inactive isomer of VD for the role of 25OHD in reducing ecDNA in HCC, as a negative control, and VD3 was used in the animal experiments. To study the effect of VD on ecDNA, we used the classical metaphase chromosome spread method to image the chromosomes of HCC cells treated with 25OHD at different concentrations; we then quantified and counted ecDNA using the image analysis tool ecSeg. The results are shown in Fig. 1, A and B. 25OHD could reduce the amount of ecDNA in a dose-dependent manner in all three HCC cell lines. PLC-PRF-5 experienced the greatest reduction in ecDNA content after VD treatment. We further used PLC-PRF-5 cell line as an example to study the dose– and time–response relationship of 25OHD reducing ecDNA. As

shown in Fig. 1C and Fig. S1E, 25OHD could reduce ecDNA in PLC-PRF-5 cells on a time-dependent basis, and the ecDNA content almost no longer decreased after 48 h. Therefore, unless otherwise specified, the processing time of 25OHD in subsequent experiments was generally 48 h. As shown in Fig. 1D and Fig. S1F, VD reduced ecDNA in PLC-PRF-5 cells in a concentration-dependent manner. When the VD concentration was 500 nM, the ecDNA level reached the lowest, and the concentration was almost no longer reduced; unless otherwise specified, we chose two concentrations of 100 and 500 nM for cell treatment. We further performed Circle-seq on HCC cells treated with 25OHD and the experimental procedure has been shown in Fig. 1E. As shown in Fig. 1F, ecDNAs larger than 10 kb were screened from the circle-seq data and 208 ecDNAs were detected in the control group wheras only 35 ecDNAs in high-dose 25OHD treated group. Gene annotation and GO analysis were performed on the reduced oncogenes carried on the ecDNA after VD treatment. As shown in Fig. 1G, the function of these ecDNA was related to EMT, proliferation, cell cycle, focal adhesion, and other malignant behaviors. From these oncogene amplifications arise, we selected two typical oncogenes (*BRAF*, *KRAS*) associated with HCC, and *SRPK1*, which had poor prognosis (Fig. S1G) and higher circle score, as representative genes for further study. As shown in Fig. 1H, the distribution of ecDNA signal at these three genes were dramatically reduced after 25OHD treatment, indicating the length of genes on ecDNA reduced and could not express the entire genes after 25OHD treatment. Taking the three genes of *BRAF*, *KRAS*, and *SRPK1* as examples, we further used fluorescence in-situ hybridization (FISH) probes in combination with matched chromosomes of centromeric probes for metaphase chromosomes and interphase cells to evaluate the amplification of these oncogenes and determine the intranuclear location of the three amplicons. To set up a positive control, junctions of ecDNA were found from the Circle-seq data (Table. S1) and CRISPR-Cas9 plasmids specifically cutting the junction of *BRAF* was designed. After 25OHD treatment, the FISH signals of all three genes were significantly reduced (Fig. 1, I and J and Fig. S1, H-K). Many clustered signals were found outside the chromosomes in the control group, reflecting a high abundance of ecDNA, whereas the signals in the 25OHD group were mainly located on the chromosomes (Fig. 1, I and J and Fig. S1H). Furthermore, the FISH signals of the three genes were also significantly reduced in PLC-PRF-5 interphase cells after 25OHD treatment (Fig. 1, I and J and Fig. S1J), indicating that 25OHD could reduce ecDNA in HCC cells. This result was also verified by qPCR of ecDNA isolated from PLC-PRF-5 cells, and the level of all three oncogenes on ecDNA decreased significantly after treatment of 25OHD (Fig. 1K and Fig. S1L). The corresponding mRNA (Fig. 1L and Fig. S1M) and protein

levels (Fig. S1N) of these oncogenes also showed a downward trend. The above results showed that 25OHD could play a role in reducing ecDNA in HCC cells, as well as decrease the transcription and translation of malignant behavior-related genes such as *BRAF*, *KRAS*, and *SRPK1*.

VD inhibits the malignant progression of HCC through ecDNA

Building on the findings of Fig. 1 that the ecDNA reduced by 25OHD was closely related to a series of malignant behaviors of HCC cells, we further verified the effect of 25OHD on inhibiting the malignant progression of HCC in vitro and in vivo. The cells did not undergo significant apoptosis after 25OHD treatment, as indicated by the results of Annexin V-PI flow cytometry (Fig. S2A). The results of scanning electron microscopy and E-cadherin/Vimentin immunofluorescence staining showed an increase in adhesion of HCC cells and an enhancement in E-cadherin expression after 25OHD treatment (Fig. 2A). Wound healing assay (Fig. 2B and Fig. S2B) and transwell assay (Fig. 2C and Fig. S2B) showed that 25OHD could reduce the migration and invasion ability of HCC cells on a dose-dependent basis. Fluorescent gelatin degradation assay showed that 25OHD inhibited the ability of degrading the extracellular matrix of HCC cells on a dose-dependent basis (Fig. 2D). To further evaluate the effect of 25OHD on HCC cells, mRNA-seq was conducted, the results showed that the mRNA levels of 2491 genes were significantly downregulated (Fig. 2E). After these downregulated genes were annotated, they were found to be associated with malignant behaviors such as invasion, EMT, and enhanced stemness (Fig. 2F). Extrachromosomal circularization and amplification are associated with increased oncogene expression. The gene expressions identified using mRNA-seq revealed that 25OHD suppressed the oncogenes coincided with ecDNAs, as confirmed by Circle-seq, suggesting that ecDNAs contribute to oncogene expression (Fig. 2G). Moreover, we integrated mRNA-seq with Circle-seq from HCC cells, revealing that genes encoded on ecDNA are among the most highly expressed genes in cancer genomes, and most of the mRNA levels of the genes which were detected in the ecDNA inhibited by 25OHD were also downregulated in the 25OHD group (Fig.2H). Therefore, the downregulation of mRNA in these genes was related to the reduction of ecDNA. We further detected markers of the relevant malignant phenotype in 25OHD-treated HCC cells, Western blot results showed a decrease in the levels of markers such as Vimentin, ZEB1 and Twist1, whereas epithelium-related marker E-cad and Occludin whereas the protein levels of epithelium-related marker were significantly increased (Fig. S2C).

To determine whether the effect of 25OHD on cell function depends on ecDNA, ecDNA was firstly purified from PLC-PRF-5 HCC cells and then subjected to linearization by sequential treatment of nickase fnCpf1 and single strand DNA-specific nuclease S1. The DNA was used as linear amplicons (liDNA) for control, and the sensitivity of ecDNA and liDNA to exonucleases Plasmid-Safe ATP-dependent DNase was verified to validate the integrity of ecDNA and successful linearization of liDNA (Fig. S2D). Equal amounts of ecDNA and liDNA were transfected into PLC-PRF-5 cells. The increase of intracellular ecDNA content after transfection verified the successfully delivery of ecDNA (Fig. S2E). As shown in Fig. 2, I and J, the malignant phenotypes such as proliferation and invasion of PLC-PRF-5 cells were enhanced after transfection of ecDNA, but there was no significant change after transfection of liDNA. The treatment of 25OHD to cells transfected with ecDNA, but not the liDNA group, counteracted the increase in malignant phenotype, indicating that the effect of 25OHD on the malignant phenotype of cells was dependent on ecDNA. Furthermore, we established two pairs of ecDNA high/low cell lines to investigate whether the effect of 25OHD on cell function depends on ecDNA. We selected a pair of high/low metastatic hepatocellular carcinoma cell lines MHCC-97L and MHCC-97H from the same patient. The ecDNA level of the two homologous cell lines was correlated with malignancy. The low metastatic cell line MHCC-97L contained a very low level of ecDNA, wheras the high metastatic cell line MHCC-97H contained a significantly higher level of ecDNA (Fig. S2F). Notably, FISH images showed oncogene amplification on ecDNA in MHCC-97H cells while in 97L cells the oncogene belonged to HSR (Fig. S2F). Functional experiments were performed separately, and the results (Fig. S2G-H) showed that the MHCC-97L cell line with low ecDNA level as well as with oncogene amplification on HSR treated with 25OHD showed no significant changes in malignant behavior such as proliferation and invasion, which suggest that the inhibitory effect of 25OHD on the malignant phenotype of hepatocellular carcinoma cells depends on ecDNA. To verify the effect of the three ecDNAs on cellular function, CRISPR-Cas9 plasmids specifically cutting the ecDNA junctions were designed (the effectiveness of plasmid knockout was validated in Fig. S10E) and transfected with PLC-PRF-5 cells. Through clone formation and gelatin degradation assay, we observed different degrees of suppression of malignant phenotypes such as cell proliferation or invasion (Fig. S2, I-J), which suggested that these oncogenes amplified on ecDNA are closely associated with tumor malignant behaviors. Next, we examined the antitumor effect of VD in vivo using the HCC orthotopic xenograft model. The results showed that VD3 inhibited the growth and metastasis of H22 xenograft tumor (Fig. 2K).

FISH was performed to evaluate ecDNA levels at tumor sites in mouse livers, consistent with the in vitro results, VD3 treated mice have significantly less ecDNA levels (Fig. 2, L and M) of the three genes, and immunohistochemistry results showed a downward trend in their protein levels (Fig. 2N and Fig. S2K). The above results showed that VD could inhibit malignant behaviors such as migration and invasion in HCC, and the anti-tumor effect of VD was related to ecDNA.

VD promotes GC nucleation to interact with DNase1L3 and stabilizes its protein levels

We further investigated the mechanism by which 25OHD reduced ecDNA. Firstly, according to the chemical structure of 25OHD, we applied three target prediction algorithms including SEA (*13*), SwissTargetPrediction (*14*), and HITPICK (*15*) to predict the possible pharmacologically active molecules targets of 25OHD. All three algorithms predicted the VDR and GC proteins with high confidence (Fig. 3A), which were supported by some research(*7*). Therefore, we knocked out these two genes using the CRISPR-Cas9 system (the effectiveness of plasmid knockout was validated in Fig. S10, A and B) to determine whether 25OHD treatment can still reduce ecDNA. After knocking out GC, but not VDR, 25OHD could not reduce ecDNA (Fig. 3B), suggesting that 25OHD reduced ecDNA mainly depend on GC. Interestingly, 1,25(OH)2D has been reported primarily activated VDR but could bind extremely weakly to GC (*16*), which further supporting the idea that VD reduces ecDNA by GC rather than VDR. After 25OHD treatment, we observed the intracellular distribution of GC protein and found that 25OHD could lead to an increase of nuclear localization of GC (Fig. 3, C and D). Western blot of whole cell lysate and nuclear lysate also showed an increase in intranuclear GC content after 25OHD treatment (Fig. 3E). Thus, we considered the degradation of ecDNA was most likely related to the increase of GC proteins in the nucleus. We then performed pulldown assay and mass spectrometry (MS) to identify the interacting protein of the intranuclear GC protein after 25OHD treatment, from which DNase1L3 (Fig. 3F) was identified. The CoIP results also confirmed that GC interacted with DNase1L3 intracellularly after the treatment of 25OHD (Fig. 3G). PLA results further showed that the increase of intracellular interaction between GC and DNase1L3 after 25OHD treatment. Notably, a significant increase in intranuclear interaction was also observed. (Fig. 3, H and I). Furthermore, we analyzed the dynamic process, free energy change, and stable conformation of 25OHD-promoted GC-DNase1L3 interactions by molecular dynamics simulations. The results are shown in Fig. 3, J to L. The Root Mean Square Deviation (RSMD) fluctuations were smaller during the

kinetic simulation compared with the solvent control system, indicating that the binding system was more stable during the kinetic simulation (Fig. 3J). The parameters of free energy, van der Waals force energy, and binding free energy of GC-DNase1L3 interactions were lower for the system containing 25OHD (Fig. 3K), indicating that the presence of 25OHD in the system led to more stable GC-DNase1L3 interactions. The images of the GC-DNase1L3 stable conformation of the intercalation region obtained from dynamic simulations are shown in Fig. 3L. The presence of 25OHD increased the amino acid residues of GC-DNase1L3 intercalation, and the distance between the two α-helices was brought closer by 2.5 Å, indicating that GC-DNase1L3 bound more tightly. To further verify the effect of 25OHD on the interactions between GC and DNase1L3, Surface plasmon resonance (SPR) and microscale thermophoresis (MST) experiments were performed. As shown in Fig. S3A, the response value of DNase1L3 was also very low at the highest concentration of GC in the PBS solution system. However, in the 25OHD solution system, the response value of DNase1L3 increased with increasing GC concentration. This finding indicates that GC and DNase1L3 protein interactions increased under 25OHD environment. In vitro MST (Fig. S3B) also showed that GC did not enhance the thermal surge of DNase1L3 in PBS environment. However, the thermal surge of DNase1L3 in 25OHD environment increased with increasing GC concentration, indicating that 25OHD promoted the interaction between DNase1L3 and GC. On the basis of the above results, we believe that GC was activated by 25OHD, which accelerated the shuttle to the nucleus and increased the chance of interaction with DNase1L3. We further investigated whether mRNA and protein levels of DNase1L3 were affected by 25OHD and GC. The results showed that 25OHD increased DNase1L3 protein level, whereas could not increase the protein level after knocking out GC (Fig. 3M). However, the mRNA level of DNase1L3 was not affected with 25OHD treatment (Fig. 3N). We also investigated whether elevated protein levels of DNase1L3 are associated with GC nucleation. Wildtype (WT) GC, nuclear localization signal (NLS)-GC and nuclear export signal (NES)-GC were designed and verified by IF (Fig. 3O). We found that the protein level of DNase1L3 in the NLS-GC group were higher than that in the wild type GC or NES-GC group. In the overexpression GC group, after 25OHD treatment, the protein level of DNase1L3 continued to increase while no increase was observed in the NLS-GC group (Fig. 3P). This result suggested that GC nucleation may be an important link in 25OHD elevating protein levels of DNase1L3. We further found that the increased GC level in the nucleus was related to the reduction of ecDNA (Fig. S3, C and D).

GC interacts with USP25 to promote the deubiquitination of DNase1L3

Previous results have shown that 25OHD treatment increases levels of the DNase1L3 protein, but not mRNA, suggesting that 25OHD did not affect the transcription of DNase1L3. Thus, we further investigated whether 25OHD affects the synthesis or degradation of the DNase1L3 protein. After the addition of protein synthesis inhibitor cycloheximide (CHX), 25OHD and NLS-GC were also able to increase DNase1L3 protein levels, whereas the addition of proteasome inhibitors MG132 did not affect DNase1L3 levels neither in 25OHD treatment group nor NLS-GC group (Fig. S4A). Thus, 25OHD inhibited the degradation of DNase1L3, resulting in the accumulation of DNase1L3. Given that the protein degradation pathway relies primarily on the ubiquitin–proteasome pathway, we investigated whether 25OHD affects the ubiquitination of DNase1L3. The results showed that the level of ubiquitination of DNase1L3 in the 25OHD and NLS-GC groups was low; after knockout of GC, 25OHD could not reduce the ubiquitination of DNase1L3, which suggested that 25OHD reduced DNase1L3 ubiquitination by GC (Fig. S4B). As this effect is associated with GC nucleation, we studied the interaction protein of GC and observed deubiquitinase USP25 in MS data (Fig. S4C). We further validated the interaction between GC and USP25 through CoIP (Fig. S4D) and PLA (Fig. S4, E and F). We suspect that the nucleated GC can recruit USP25 near DNase1L3 so that the ubiquitination of DNase1L3 was removed. As a result, we further investigated whether USP25 can remove the ubiquitination of DNase1L3. After overexpression of USP25, the ubiquitination of DNase1L3 was reduced (Fig. S4G) and the half-life significantly improved (Fig. S4, H and I), whereas the ubiquitination level of DNase1L3 increased (Fig. S4J) and the degradation became faster after knocking out USP25 (Fig. S4, K and L).

DNase1L3 degrades ecDNA in vitro and in vivo

GC interacts with DNase1L3 after activated by 25OHD and localized into nucleus. We were concerned about whether DNase1L3 is closely related to the degradation of ecDNA. Firstly, metaphase chromosome spread method, imaging by DAPI staining, followed by ecSeg analysis, was applied to detect ecDNA. The results showed that transfection of DNase1L3 plasmid or protein reduced the content of ecDNA, whereas an increased level of ecDNA was detected after knocking out DNase1L3 (Fig. 4, A and B). We further studied the FISH signals of *BRAF*, and the results also showed that the ecDNA content decreased after transfection of plasmids or proteins of

DNase1L3 in both metaphase spreads and intaphase HCC cells (Fig. 4, C to E). The results of qPCR of isolated ecDNA were also consistent with the data of FISH (Fig. 4F). The rest of the two oncogenes were also verified in Fig. 4, G to I and Fig. S5, A and B. To confirm that these results were caused by the direct interaction of DNase1L3 with ecDNA, excluding indirect effects, we also designed in vitro experiments for verification. After the extraction of genomic DNA, Plasmid-Safe ATP-dependent DNase was added to eliminate linear chromosomal DNA to purify circular DNA. DNase1L3 protein was added to the reaction containing ecDNA with the presence of Ca^{2+} and Mg^{2+} and incubated at 37 °C; the DNA content was found to be greatly reduced (Fig. 4J). We further studied the quantitative efficacy (Fig. 4K) and timeliness (Fig. 4L) of DNase1L3, and the results showed that its efficacy and timeliness were significantly linearly correlated (R^2>0.75, P=0.0001). Nearly 90% of ecDNA was degraded after 1 h of 40 ng/μL DNase1L3 or 2 h of 10 ng/μL DNase1L3, but the degradation efficiency was low when the solution system was alkaline (pH=8) (Fig. 4M). We also examined the degradation preference of DNase1L3 on linear DNA versus ecDNA. As shown in Fig. 4N, DNase1L3 degraded both forms of DNA, and the degredation effect for ecDNA was better for the same incubation time and concentration. Here, we also made a comparison among DNase1, an endonuclease from human, and micrococcal Nuclease (MNase), an endonuclease from Staphylococcus aureus, and DNase1L3 to evaluate the degradation effect on ecDNA. As shown in Fig. 4O, the degradation of ecDNA by DNase1 was weaker than that by DNase1L3, and the degradation of ecDNA by MNase, a widely used enzyme in ChIP experiments, was strongest. The ecDNA levels slightly decreased for either the mutant DNase1L3 (R206C) or the addition of zinc chloride to the DNase1L3 solution.

DNase1L3 affinitizes lipid droplets through lipophilic regions and degrades the ecDNA surrounded by lipid droplets

We further investigated the spatial properties of DNase1L3 to degrade ecDNA. Imaging with structured light illumination microscopy (SIM, Fig. 5A), it showed that *BRAF* ecDNA in PLC-PRF-5 cells was clustered rather than diffuse, which was consistent with the ecDNA distribution characteristics reported previously (*17*). DNase1L3 and ecDNA were highly co-localized after 25OHD treatment, with a colocation coefficient of more than 0.5. In particular, large DNase1L3 signals were also found in ecDNA hubs. Fluorescence statistics of the ecDNA-enriched regions showed that the signals of ecDNA and DNase1L3 in the two groups always appeared at the same

time. The ecDNA signal in the Control group was stronger than that of DNase1L3, while the ecDNA signal in the 25OHD group was weaker than that of DNase1L3 (Fig. 5B). The signal of ecDNA was greatly reduced after treatment of 25OHD, and the clustering phenomenon almost disappeared (Fig. 5C). The presence of the DNase1L3 signal near ecDNA suggested that 25OHD may have helped DNase1L3 better recognize and degrade ecDNA. 25OHD is a lipid-soluble molecule, so we analyzed the charge distribution of DNase1L3. As Fig. 5D shows, outside the enzyme viable region of DNase1L3 was an electrically neutral domain at the N-terminal (NT), which is a lipophilic region. Therefore, we further investigated whether degrading ecDNA by DNase1L3 is related to lipophilicity.

DNase1L3 and lipid droplets (LDs) were co-stained with immunofluorescence and the chemical dye BODIPY for SIM imaging. As shown in Fig. 5E, we found LDs in the nucleus, where individual LDs were close in size to the cytoplasmic LDs, and micro-LDs occupied the majority. A magnified image of the LDs locally (bottom left), as well as a signal that enlarged the overlap part of DNase1L3 and LD in the image (bottom right), provided a better view of the LDs and their interaction with DNase1L3. In the 25OHD group, the overlapping signal of LDs and DNase1L3 was the strongest. Further statistical analysis is shown in Fig. 5F. After 25OHD treatment, there was no significant change in the number of LDs, but the area of LDs increased significantly compared with the control group, whereas the signal of DNase1L3 in the LDs increased significantly. Cells were treated with Oleic acid and forskolin which were reported as lipid droplet inducer and inhibitor respectively, we observed that the number of cytoplasmic LDs and intranuclear LDs increased after oleic acid treatment while a decrease was observed after forskolin treatment. However, neither oleic acid nor forskolin changed the signal intensity of DNase1L3 in the LDs, suggesting that the number of LDs did not affect the interaction with DNase1L3. Therefore, DNase1L3 is more affinitive for LDs in the present of 25OHD. Since DAPI signals were found in the LD from SIM microscopy images, we further investigated correlation of ecDNA and LDs.

We visualized ecDNA containing *BRAF* by FISH and LDs were stained with BODIPY and signals were observed with SIM microscopy. Given that the FISH procedure breaks up large LDs within the cytoplasm, we first confirmed that the microLDs in the nucleus were not affected by the FISH experiment. In Fig. 5G, *BRAF* FISH results showed that microLDs were near ecDNA, and there was a strong overlap between microLDs and ecDNA in the 25OHD-treated cells.

However, the oleic acid and Forskolin treatments did not significantly affect the overlap between microLDs and the amount of ecDNA (Fig. 5, H and I), suggesting that the number of LDs did not affect the formation or degradation of ecDNA. However, microLDs were observed near ecDNA. The above results implied that LDs might be related to ecDNA degradation. We further investigated whether the action of DNase1L3 is related to LDs, for which we designed three DNase1L3 tracer plasmids shown in Fig. 5J: Wild type DNase1L3(WT), DNase1L3 with lipophilic region deleted (ΔNT), and DNase1L3 with three repeated segments of lipophilic region (3×NT) at the N-terminal. The plasmids were transfected to cells respectively and co-stained with BODIPY to perform SIM ultra-high resolution live cell imaging. As shown in Fig. 5, K and L, DNase1L3$^{\Delta NT}$ hardly entered the LDs, whereas DNase1L3$^{3\times NT}$ increased the interaction with LDs compared with WT. The results of Western blot on proteins in lipid droplets also coincide with cell imaging (Fig. S6A). These results suggested that the NT region of DNase1L3 is crucial for the interaction with LDs, helping DNase1L3 to access ecDNA clusters surrounded by LDs to function as a degrader. We also proved that DNase1L3$^{3\times NT}$ degraded ecDNA better (Fig. 5M).

It has been reported that DNase1L3 plays an important role in the apoptotic process (*18*). We further investigated why DNase1L3 is able to cleave DNA but does not directly lead to apoptosis. DNase1L3 activity could be inhibited by poly(ADP-ribosyl)ation (PARylation) in DNA degradation (*19*) . We found that almost no PARylation of DNase1L3 occurred in lipid droplets, but most cellular DNase1L3 was in PARylation state, as determined by Western blot and Co-IP experiments (Fig. 5, N and O). When we transfected PARP1 with a 3× lipophilic region, we forced PARP1 (the writer of PARylation) to be close to DNase1L3 on the lipid droplet, so DNase1L3 on LD was again modified by PARylation (Fig. 5P), and the ecDNA level in the cells was increased (Fig. 5Q). This finding suggests that LD can protect DNase1L3 from PARylation, which may be the key for DNase1L3 to degrade ecDNA around lipid droplets but not genomic DNA under specific spatial and temporal conditions. 25OHD enlarges LD, increases the amount of DNase1L3 in LD, and also protects DNase1L3 from interacting with PARP1, making DNase1L3 in lipid droplets more susceptible to degradation of ecDNA. The results of SIM images (Fig. S6B) also support this conclusion.

We further investigated the effect of GC on the interaction of DNase1L3 with LDs. We first observed the localization of GC and DNase1L3 in LDs after 25OHD treatment using immunofluorescence staining. The results showed that 25OHD increased the GC and DNase1L3

in LDs (Fig. S6C). We extracted LD after overexpressing GC in cells and detected the content of DNase1L3 in LD. As shown in Fig. S6D, the content of DNase1L3 in the equivalent lipid droplets increased after the overexpression of GC. After extracting LD from cells treated with 25OHD, the contents of GC and DNase1L3 in the equivalent LDs increased. The results indicate that GC interacts with DNase1L3 to increase DNase1L3 bind to LD. We also constructed the GC-DNase plasmid as shown in Fig. S6E, that is, GC and DNase1L3 were artificially connected. The SIM results showed that VD enhanced the interaction signal and area of DNase1L3 with LDs, and the interaction signal and area between GC-DNase and LDs were also stronger than DNase1L3 (Fig. S6, F and G). Therefore, we further performed ecDNA degradation assay (Fig. S6H) to simulate lipid droplet environment in vitro, i.e., adding liposome to the reaction of Fig.4 The results show that the simultaneous addition of GC and liposome could substantially enhance the degradation of ecDNA by DNase1L3, consistent with the in vivo phenomenon that the GC activation of DNase1L3 is dependent on lipid droplets. The above results showed that 25OHD promoted the recognition of DNase1L3 and LDs, and this effect was dependent on GC. 25OHD interacted with DNase1L3 after binding GC, making DNase1L3 more lipophilic and helping degrade ecDNA.

DNase1L3 inhibits the malignant progression of HCC dependent on lipophilic regions

Given that DNase1L3 has the effect of degrading ecDNA of HCC cells, and this effect depends on its lipophilic region (NT), we further investigated the effect of DNase1L3 in inhibiting the malignant progression of HCC in vivo and in vitro and determined whether its role is related to the lipophilic region. SEM images showed that the epithelial morphology of HCC cells in the overexpressed DNase1L3, 3×NT group were more pronounced and the adhesion increased compared with the control group. However, ΔNT group did not show obvious changes. The immunofluorescence of EMT key markers E-cadherin and Vimentin also showed the same trend (Fig. 6A). Thus, DNase1L3 may be able to inhibit malignant behaviors such as EMT in cancer cells, and this effect depends on its NT lipophilic regions. Since DNase1L3 has been reported to be associated with apoptosis(*20*), we investigated whether the antitumor effect it exerted in HCC was a consequence of the induction of apoptosis, as indicated by the result of Annexin V-PI flow cytometry in Fig. S7A, the cells did not undergo significant apoptosis after over expression or knock out of DNase1L3.Wound healing assay, transwell assay (Fig. 6, B and C, and Fig. S7B), and fluorescent gelatin degradation assay (Fig. 6, D and E) showed that DNase1L3 could inhibit

the migration and invasion ability of HCC cells, but the deletion of NT did not show an obvious effect, indicating that this function was dependent on NT. EMT related marker also showed the same trend of changes (Fig. 6F). The pair of ecDNA high/low cell line were applied to investigate the effect of DNase1L3 on cellular functions including clone formation, migration, and invasion. Fig. S7, C-D shows that the MHCC-97L cell line with low ecDNA level and with oncogene amplification on HSR itself after overexpression of DNase1L3 had no significant changes in malignant behavior such as proliferation and invasion. Hence, DNase1L3 is not functionally significant for cancer cells with only HSR amplification in contrast to those with high ecDNA levels. Animal studies of orthotopic liver xenograft tumors also showed that DNase1L3 inhibited the growth of H22 xenograft tumor (Fig. 6, G and H) and prolonged the survival of tumor-baring mice (Fig. 6I), which relied on its NT lipophilic regions. The pathological sections of the tumor site of the mouse liver were subjected to FISH, and the ecDNA level was evaluated. After in situ transplantation of cells overexpressing DNase1L3$^{3\times NT}$, the ecDNA levels of *BRAF*, *KRAS*, and *SRPK1* were significantly reduced (Fig. 6J and Fig. S7E), and the corresponding protein levels were also significantly reduced (Fig. 6K and Fig. S7F). However, no significant differences were found in the overexpression ΔNT group. The above results showed that DNase1L3 degraded ecDNA in vivo, exerted antitumor effects, mainly relied on its NT lipophilic regions.

Based on these findings, we further studied the pivotal role of DNase1L3 and GC on the anti-tumor effect of 25OHD. The results of scanning electron microscopy and E-cadherin/Vimentin immunofluorescence staining showed an increase in adhesion of HCC cells and an enhancement in E-cadherin expression after 25OHD treatment, whereas the function which 25OHD exerted disappeared after knocking out of DNase1L3 or GC in HCC cells (Fig. S8A). Wound healing assay (Fig. S8B), transwell assay (Fig. S8C), and fluorescent gelatin degradation assay (Fig. S8, D and E) showed that 25OHD could inhibit the migration and invasion ability of HCC cells, but the knockout of DNase1L3 or GC did not show an obvious effect. Animal studies of orthotopic liver xenograft tumors revealed that knock out of DNase1L3 or GC dramatically increase the growth of H22 xenograft tumor (Fig. S8, F and G) and shorten the survival of tumor-baring mice (Fig. S8H). Collectively, these findings suggested the anti-tumor effect of 25OHD depend on DNase1L3 and GC.

DNase1L3-related mRNA drugs have the potential therapeutic effects on the clinical treatment of HCC

mRNA drugs have emerged as a therapeutic strategy such as COVID-19, and some studies have shown that the use of mRNA drugs to deliver tumor suppressor genes is a promising treatment for cancer (*21*). Given that the DNase1L3 we found has the nature of a tumor suppressor gene, we used TCGA data to perform pathological analysis of DNase1L3 expression in patients with HCC. The expression of DNase1L3 in HCC was extremely low compared with that in adjacent normal tissues (Fig. 7A). Patients with liver cancer with high DNase1L3 expression had a longer overall survival and disease-free survival (Fig. 7B). The higher the pathological grade and clinical stage, the lower the expression of DNase1L3 (Fig. 7C). The above results showed that DNase1L3 demonstrated pathological significance in HCC, so we also considered preparing DNase1L3 as an mRNA drug and evaluating its effect using eight PDX models (Fig. 7D). We also evaluated the efficacy of GC-DNase mRNA drugs. The PDX models showed that both DNase1L3 and GC-DNase mRNAs were able to inhibit tumor growth (Fig. 7E) and prolong survival in mice (Fig. 7F). FISH was performed on the pathological slices of the tumor site, and the ecDNA level was evaluated. After the treatment of the two mRNAs, the ecDNA levels of *BRAF*, *KRAS*, and *SRPK1* were significantly reduced (Fig. 7, G and H). IHC results showed that the expression of malignantly associated proteins such as BRAF, KRAS, and SRPK1, and Vimentin decreased, whereas the expression of E-cadherin increased (Fig. 7, I and J).

Considering that DNase1L3 may be a tumor suppressor gene, we evaluated the effect of DNase1L3 deletion on liver organoid formation using human induced pluripotent stem cells (iPSCs)-derived liver organoids. After knocking out of DNase1L3 using lentivirus (the effectiveness of knockout was validated in Fig. S10F) three days before hepatic organoid maturation, the morphology of the liver organoid gradually became disordered, the normal hepatic organoids (Fig. S9B) could not be formed, the liver-specific marker ALB was no longer expressed, and the liver-specific antibody hepatocyte stain was also negative (Fig. S9C). On the basis of the DEN-induced HCC model, we found more tumors in the AAV8-encapsulated ko DNase1L3 plasmid group (the effectiveness of knockout was validated in Fig. S10, G and H) than in the control group (Fig. S9D). Thus, DNase1L3 may be a gene needed for liver development and critical for maintaining a normal state of liver, while the deletion of DNase1L3 may lead to tumor formation.

Discussion

In recent years, a large number of research results on ecDNA have greatly deepened our understanding of cancer, as well as DNA and gene expression. The distribution and content, structure, formation, and function of ecDNA and other basic issues have been reported in the literature, but information on the degradation mechanism of ecDNA and drug interventions is lacking. In this study, we found that DNase1L3 was an important protein for degrading ecDNA, and we verified the important role of DNase1L3 in cells, animals, organoids, and PDX models. Supplementation with DNase1L3 may be a potential anti-tumor therapy. DNase1L3 inhibits proliferation, invasion, and metastasis of HCC.(*22*) This study also showed a strong association between DNase1L3 and the clinicopathology of HCC, which is a factor with good prognosis. This study explained the mechanism by which DNase1L3 inhibits tumor progression from the perspective of degrading ecDNA.

Studies have found that the absence of DNase1L3 is prone to systemic lupus erythematosus (*23*), and this study can also explain this phenomenon. We found that DNase1L3 could degrade circular DNA, and eccDNA has been shown to have strong immunogenicity (*20*). Deletion of DNase1L3 may result in circular DNA not being cleared by cells, thereby becoming an immunogen and mediating or exacerbating the onset and progression of systemic lupus erythematosus. (*24, 25*). Mice with DNase1L3 deletion have been found to have an increase in short DNA molecules below 120 bp in plasma and long, multinucleated small body DNA molecules (*26*). This phenomenon may also be related to DNase1l3 deletion.

Interestingly, Zhang et al. found that DNase1L3 in mouse embryonic stem cells is also involved in the formation of eccDNA (*20*). The study found that eccDNA was produced during apoptosis. DNase1L3 cleaves DNA during apoptosis, producing apoptotic DNA fragments that are connected by DNA ligase 3 to eccDNA. Our study found that DNase1L3 could degrade ecDNA, but this did not contradict this study. It has been reported that DNase1L3 activity could be inhibited by PARylation in DNA degradation (*19*). Under normal conditions, a large amount of PARylation writing enzyme PARP1 is present in cells, so DNase1L3 is mostly in a PARylation state, i.e., inhibited, and therefore cannot cleave DNA and does not induce apoptosis. Under the induction of inflammatory factors or other apoptosis inducers, PARP1 enzyme is cleaved by Caspase-3 and is then inactivated, which is the classical apoptotic pathway. In this pathway, PARP1 inactivation leads to DNase1L3 no longer being in PARylation state, so DNase1L3 is activated and cleaves

DNA, eventually forming a DNA ladder. In this work, we found that almost no PARylation of DNase1L3 occurred in LDs, and LDs can protect DNase1L3 from being modified by PARP1, which may be the key for DNase1L3 to degrade ecDNA around lipid droplets but not genomic DNA under specific spatial and temporal conditions. VD/GC promoted DNase1L3 enrichment in lipid droplets and probably also protected DNase1L3 from PARylation by PARP1 through spatial site blocking, allowing DNase1L3 in lipid droplets to remain active and more susceptible to the degradation of ecDNA.

We found that the lipophilic region of DNase1L3 played an important role in affinity ecDNA, suggesting that lipid droplet protection may be one of the reasons why ecDNA was not easily degraded. In this study, SIM microscopy was used to determine the distribution of micro-LDs in the nucleus around ecDNA, as well as examine the interaction of DNase1L3 with LDs. For a long time, LDs were thought to be mere cytoplasmic inclusions of fat. In recent years, LDs have received widespread attention from the biological community and have been recognized as intact organelles with key functions in lipid and energy homeostasis.(*27*) However, the study of its function mainly focuses on the role of large LDs in the cytoplasm in the process of lipid metabolism, storage, and signaling, and there is less research on LDs in the nucleus is limited. The presence of LDs in the nucleus and their biogenesis processes have been observed and studied in the literature(*28-30*), but the function of LDs in the nucleus has not been studied in depth. Nucleolipid droplets have been found to regulate the synthesis of phosphatidylcholine(*31*). Our results suggested that intranuclear LDs may be closely related to the behavior of DNA. Specifically, in this study, we found that VD-GC increased the binding of DNase1L3 to LDs by interacting with DNase1L3, which may be a liver-specific pathway, and that there may be other mechanisms with similar effects. The relationship between intranuclear LDs and ecDNA, and whether LDs are involved in transcriptional regulation, must be further studied.

VD has a wide range of health benefits, including reducing the risk of various types of tumors, T2DM, and cardiovascular disease; such benefits have been supported by substantial clinical evidence(*32*). However, the mechanism of the anti-tumor effect of VD is not well studied, and the biological function of VD is mainly mediated by binding to VDR(*7*). The vitamin D–VDR complex binds to the VD response elements (VDREs) on the promoters of target genes and regulates their expression.(*33*) VD inhibits the adhesion and proliferation of cancer cells by suppressing THBS1 via VDR/Smad3 competition (*34*). We demonstrated experimentally that VD

can physically enhance the interaction of DNase1L3 with GC and demonstrated the triple action of GC on DNase1L3. (1) Quantity: GC enters the nucleus and interacts with DNase1L3 under the action of VD, recruiting USP25, deubiquitinating DNase1L3, inhibiting DNase1L3 degradation, and ensuring the protein level of DNase1L3. (2) Spatial: VD enhances the hydrophobicity of the GC/DNase1L3 interaction structural domain, making it more susceptible to lipid droplet adsorption, drawing it closer to ecDNA, and becoming more easily degraded ecDNA (spatial). (3) Activity: GC makes DNase1L3 less susceptible to PARylation and activation by promoting lipid droplet adsorption and spatial site blocking. VD/GC enhances the degradation of ecDNA by affecting three aspects: quantity, spatial distribution, and DNase1L3 activity. Only VD forms that can bind to GC can degrade ecDNA, which exhibits a strict GC-dependent feature. 1,25-Dihydroxyvitamin D cannot bind GC, and experiments have shown that it cannot reduce ecDNA. Therefore, the effect of VD on ecDNA, which is not significantly associated with its involvement in calcium metabolism as a vitamin, is a novel ligand-like regulatory molecular mechanism. Given that ecDNA can explain the heterogeneity of tumors, this mechanism can also explain why VD can play a distinguished role of prevention and treatment among many cancer types. VD can promote the degradation of ecDNA, and this role may also explain the clinical conclusion that VD can reduce the incidence of autoimmune diseases (*35*). Compared with DNase1L3 and GC-DNase, the effect of VD degradation of ecDNA, although indirect, is more economical and more available, and appropriate supplementation of VD in patients with cancer still has strong clinical significance. Despite few reports of VD combining with other therapies to fight tumors, some studies believe that VD has add-on value in patients with breast cancer receiving doxorubicin-based chemotherapy. Chemotherapy is thought to lead to the accumulation of ecDNA, and this study provided a theoretical basis for the combination of VD and chemotherapy drugs. Whether VD can be combined with targeted drugs and immunotherapy in the future also needs to be studied, and this study is believed to provide theoretical reference for future related therapies (Fig. 7K).

Frankly speaking, there are some limitations to this work. The functions of cancer cells affected by overall or multiple ecDNAs are difficult to evaluate directly and only the knockout of junction sequences can be used to achieve the intervention of individual ecDNA due to the limitation of ecDNA research methods when studying the influence of ecDNA on cancer cell behaviors. Secondly, in the aspect of pharmacology, the clearance of ecDNA by VD is dependent on GC and DNase1L3, there is a matter of dose saturation, which also limits the anti-tumor effect of VD. Accordingly, further research is needed in the future to investigate pathways that allow

DNase1L3 to increase or enhance its activity to compensate for this deficiency. Furthermore, the present work identified the role of lipid droplets in degrading ecDNA and also showed that lipid droplets have a double-edged character in cancer cells, which needs to be further investigated. The lipid metabolic status and VD/GC/DNase1L3 levels differ considerably in different tumor types. This study was conducted with hepatocellular carcinoma as an example, and other types of tumors need to be studied in depth. The clearance mechanism of ecDNA identified in this work has potential implications for drug resistance tumors, immunotherapy and developmental biology. Nevertheless, these issues have not been addressed in this work and further study is needed.

Methods and Materials

Cell culture

The human HCC cell lines Hep3B was obtained from the Guangzhou CELLCOOK, SK-Hep1, PLC-PRF-5 were purchased from Nanjing Keygen Biotech. MHCC97-L, MHCC97-H and H22-Luc were purchased from Shanghai Zhong Qiao Xin Zhou Biotechnology. SK-Hep1 and H22-LUC cells were cultured in RPMI-1640 medium (Keygen Biotech), and Hep3B, PLC-PRF-5, MHCC97-L and MHCC97-H cells were cultured in Dulbecco's modified Eagle's medium (Keygen Biotech) supplemented with 10% (v/v) fetal bovine serum (Thermo Fisher) at 37°C in humidified atmosphere containing 5% CO_2. The cell lines were tested to determine the presence of Mycoplasma before use. Complete cell identification was provided by CELLCOOK or KeyGen Biotech.

Plasmids construction and Overexpression and CRISPR knockout

The DNase1L3$^{\Delta NT}$ sequence was obtained by deleting the N-terminal lipophilic region sequence (NT, MSRELAPLLLLLLSI) and the C-terminal DYK sequence of the DNase1L3 protein coding sequence from the DNase1L3_OHu20141D_pcDNA3.1+/C-(K)-DYK plasmid (Genscript). The obtained sequence was then inserted into the pmEGFP-N1 vector to construct DNase1L3$^{\Delta NT}$-EGFP. DNase1L3$^{3\times NT}$-EGFP was constructed by adding three lipophilic region repeats (3×NT, MSRELAPLLLLLLSIMSRELAPLLLLLLSIMSRELAPLLLLLLSI) to the N terminus of the DNase1L3 protein coding region and deleting the C-terminal DYK sequence from the DNase1L3_OHu20141D_pcDNA3.1+/C-(K)-DYK plasmid (Genscript), followed by insertion into the pmEGFP-N1 vector. The GC-DNase plasmid was obtained by deleting the sequence of the N-terminal lipophilic region, as well as the C-terminal SSRAFTNSKKSVT and DYK tags of DNase1L3 from the DNase1L3 _OHu20141D_pcDNA3.1+/C-(K)-DYK plasmid. The obtained sequence was inserted into the GC_ OHu14110D_pcDNA3.1+/C-(K)-DYK plasmid at the C-terminus of the GC protein coding region, with insertion of linker GGGGSGGGGSGGGGS between the two sequences to achieve fusion expression of GC and DNase1L3 proteins. Information about these plasmids is also provided in the Materials table.

PLC-PRF-5 cells were transfected using Lipo8000 (Beyotime) according to the manufacturer's instructions with Flag-DNase1L3, Flag-GC, and Flag-USP25, DNase1L3-EGFP, DNase1L3$^{\Delta NT}$-EGFP, DNase1L3$^{3\times NT}$-EGFP, NLS-GC, NES-GC, Flag-PARP1, GC-DNase-EGFP overexpression plasmid or CRISPR Knockout Plasmids containing Cas9 and guide RNAs of GC,

VDR, DNase1L3, and USP25. Transfected cells were incubated for 48 h before puromycin selection. GC, VDR, DNase1L3, and USP25 knockout were confirmed by western blotting.

Cell proliferation assay

At 0, 12, 24 and 48 hours after treatment, cell viability were measured by Cell Counting Kit-8 (CCK8, Beyotime). Cell culture medium was removed and 10 μL of CCK8 solution was added to each well of a 96-well plate. Afterward, the cells were incubated for 1 hour at 37°C in 5% CO_2. Absorbance was measured at a wavelength of 450 nm using an ELISA microplate reader (Thermo Fisher). Assays were repeated at least three times.

Cell apoptosis

After 48 hours, cells were harvested with 0.25% trypsin without EDTA. They were also washed twice with ice-cold phosphate-buffered saline (PBS), resuspended in 250 mL of binding buffer, adjusted to 1×10^6 /mL, and fixed in 1% paraformaldehyde. Subsequently, they were stained with the Annexin V/PI Apoptosis Detection Kit (KeyGen Biotech). They were analyzed with a flow cytometer (Millipore) after incubation in the dark for 30 min.

Colony formation assay

Colony formation was performed in 6 cm culture dishes (Corning). Totally 600 cells were seeded per dish and cultured for 14 days. Colonies were fixed in methanol for 10 min and stained with 0.1% crystal violet for 30 min at room temperature. The number of colonies was counted by ImageJ.

Wound healing assay

Cells were seeded and cultured in a 6-well plate, and the cell density reached an appropriate level. Use a sterile pipette tip to evenly scrape the cells for a scratch test. Add serum-free medium and use live cell imaging for 12, 24, and 48 hours respectively. The cell migration was photographed and measured, and analyzed by ImageJ.

Transwell

Matrigel (Corning, 354234) was diluted in DMEM at a ratio of 1:8, 1×10^5 cells were seeded into a 24-well Transwell chamber (JET, TCS013024) covered with matrigel and then incubated at 37 °C for 48 hours. Approximately 1×10^5 cells were seeded onto the Matrigel and then incubated at 37 °C for 48 hours. 0.1% crystal violet was used to stain the invasive cells on the lower surface of the chamber. Images were taken by using a phase-contrast microscope.

Gelatin degradation assay

Prepare pork skin gelatin (Thermo Fisher, G13187) diluted with 2% sucrose in PBS. Gelatin was used at a final concentration of 0.2 mg/mL. The working solution is protected from light and heated

to 60°C to cover the slides evenly, after drying, add 1 mL of a pre-chilled solution of glutaraldehyde and incubate for 15 minutes on ice. Wash coverslips three times at room temperature with PBS. Add 1 mL of a freshly prepared solution of Sodium Borohydride and incubate for 3 minutes at room temperature. Inoculate cells and culture for 24 hours. Images were acquired on the ZEISS LSM 800 Inverted Confocal microscope attached with an Airyscan area detector.

Pull down

PLC-PRF-5 cells expressed Flag-GC were harvested in lysis buffer (50 mM Tris-HCl, pH7.5, 100 mM NaCl, 5 mM $MgCl_2$, 0.5% Triton, protease inhibitor cocktail). Anti-Flag tag affinity beads (Beyotime) were used to incubate with the cell lysates extracts for 12 hours at 4°C. After binding, wash the beads with lysis buffer (3×10 minutes). And then elute the Flag protein complex. The eluates were gathered and visualized by Western blotting.

Silver staining

Protein eluates were collected by pull-down assay. The 10% SDS-PAGE was used to separate proteins, and the electrophoresis were performed with a constant voltage (80 V for concentrated glue, 120 V for separated glue) in the running buffer until the dye front reached the lower end of the gel (2 hours). According to the manufacturer's manual, the gel was silver stained under shaking with Fast Silver Stain Kit (Beyotime).

LC-MS/MS

The target bands on SDS-PAGE were collected and cut into approximately 1 mm^3 size, decolorized by adding 200 μL of 50 mM NH_4HCO_3 /50% acetonitrile in a centrifuge tube and shaking for 10 min at 37 °C, until the gel becomes transparent. Add 200 μL acetonitrile and wash the gel 2 times. Subsequently dry it at 37 °C for 15 min at 300 rpm. Add 100 μL of 10 mM dithiothreitol and shake at 56 °C for 45 min at 400 rpm. After that, add 200 μL of acetonitrile to wash the gel. Discard the liquid in the tube and immediately incubate the gel by adding 100 μL of iodoacetamide at room temperature and protected from light for 30 min. Sequentially add 200 μL of 50 mM NH_4HCO_3/50% acetonitrile, 100% ACN to wash the gels. Dry the gel and incubate it by adding 100 μL of 10 ng/μL trypsin (Thermo Scientific, 90057) at room temperature for 1 min, followed by ice bath for 5 min.The supernatant was removed by centrifugation at 13000 rpm for 30 s. 200 μL 25 mM NH_4HCO_3 was added to incubate the gel at room temperature for 1 min, followed by an ice bath for 10 min. Overnight incubation was conducted at 300 rpm at 37 °C. After completion, 200 μL of 1% formic acid 2% acetonitrile-H_2O solution, 50% acetonitrile-H_2O solution and 50 μL of 1%

formic acid-acetonitrile solution were added sequentially to the original tube of gel, shaken thoroughly and sonicated for 10 min. The purified tryptic peptides were analyzed by LC-MS/MS retrieval.

Western blotting

Cell lysates were collected, and the protein levels were quantified using a standard BCA assay kit (Thermo Fisher, 23227). Proteins were separated by 10% SDS-PAGE gel and transferred onto PVDF membranes (Millipore). After blocked in 5% skim milk for 2 hours, the membranes were incubated with primary antibody at 4°C overnight, and then incubated with horseradish peroxidase-conjugated goat anti-rabbit or goat anti-mouse IgG secondary antibody (Beyotime) for 2 hours at room temperature. Membranes were washed 3 times with TBST for 10 minutes. Protein expression was assessed using an enhanced chemiluminescent substrate (Affinity) and exposed to a chemiluminescent film.

Co-IP assay

For Immunoprecipitation, 50 μL of Protein A/G agarose (Beyotime, P2012) was incubated with antibodies against GC, DNase1L3, USP25 overnight at 4°C with continuous rotation. The lysates were centrifuged at 12000 rpm for 10 minutes at 4°C, and then incubated with the antibody-conjugated beads overnight at 4°C. After incubation, washed the beads three times with cold lysis buffer. The precipitated proteins were separated from the beads by resuspending the beads in 1×SDS-PAGE loading buffer and boiling at 99°C for 10 minutes. Consequently, the boiled proteins were analyzed by Western blotting.

Quantitative PCR

Total RNA of HCC cells was extracted using Trizol reagent (Invitrogen, 15596026) in accordance with the manufacturer's instructions. cDNA was obtained by a FastQuant RT kit (TIANGEN, R6906). Transcript quantification was performed by a SYBR green kit (TIANGEN, FP205). The samples were run in triplicate in each experiment. The $2^{-\Delta\Delta CT}$ method was applied to quantify relative gene expression. The qRT-PCR primers are listed in the Materials table.

Protein expression and purification

Flag-Tagged DNase1L3, Flag-Tagged GC, plasmids were overexpressed in HEK293F cells. Cells were then grown to optical density of 1.2×10^6 cells/mL at 37 °C and transfected with Flag-Tagged plasmids using PEI (Polysciences, 23966-2). After 48 h of transfection, cells were harvested by centrifugation at 800g. The collected cells were resuspended lysis buffer [50 mM tris-HCl (pH 7.4), 150 mM NaCl, 1 mM EDTA, 0.5%TrittonX-100, 10% Glycerol, protease inhibitor cocktail

(TargetMol)] and were lysed by sonication for 2 hours at 4°C. The supernatant was collected by centrifugation at 120,000g for 60 min at 4°C and then incubated with anti-DYKDDDDK Magnetic Beads (Genscript, L00835) for 1 h at 4°C. Wash the beads for 3 times using lysis buffer, proteins were eluted with competitive DYKDDDDK peptide (Genscript, RP10586).

Surface plasmon resonance (SPR) assay

SPR experiments were performed using a BIACORE T200 instrument (GE Healthcare, GER) at 25°C. DNase1L3 protein were immobilized on CM5 sensor chips using the Biacore Amine Coupling Kit in accordance with the manufacturer's instructions. Briefly, the chip was activated using a 1:1 mixture of 0.2 M N-ethyl-N′-(3-dimethylaminopropyl) carbodiimide and 0.05 M N-hydroxysuccimide at 10 μL/min for 7 min. DNase1L3 was coated on the chip at 150 μg/mL in 10 mM sodium acetate buffer (pH 5.0). GC protein was diluted to 20 μg/ml by 1×PBS (pH 7.4). Finally, a series of GC from 0–220 nM was used as kinetic analytes. 1×PBS (pH 7.4, 0.1% DMSO) was used as the running buffer for analyte dilution. All buffers were filtered and degassed prior to use and the data were analyzed using the BIA evaluation software (Version 4.1).

Microscale thermophoresis

Proteins were labelled with the cysteine-reactive dye Alexa Fluor 488 C5 maleimide (Thermo Fisher). Purified DNase1L3 protein was incubated with ~20-fold molar excess of the dye in gel-filtration buffer for 30 min. After labelling, the excess dye was removed by applying the sample on Superdex 200 column equilibrated with the gel filtration buffer. Tween 20 (0.05%) was added to the protein buffer for microscale thermophoresis measurements before the experiment.Datasets were collected at a temperature of 25°C. For the Alexa Fluor 488-labelled DNase1L3 interaction with GC, a concentration series of GC was prepared using a 1:1 serial dilution of GC in PBS buffer. The range of GC concentration used was from 28 μM to a final concentration of 0.85 nM, over 16 serial diluted capillaries with 10 μL samples. The interaction was initiated by the addition 10 μL of 400 nM Alexa Fluor 488-labelled DNase1L3 to each reaction mixture, resulting in a 200 nM final concentration of DNase1L3. The LED power was 100% and the microscale thermophoresis power (that is, the power supplied to the infrared laser) was 60%. The pre-microscale thermophoresis period was 5 s, the microscale thermophoresis acquisition period was 20 s, and the post- microscale thermophoresis period was 5 s. Data were analysed by MO Control software provided by NanoTemper.

Extraction of ecDNA based on alkaline lysis

Crude ecDNA was first extracted from 1×10^7 HCC cells by alkaline lysis（PMID:34671165）, Then, linear contaminant DNAs within the crude circular DNA are digested with Plasmid-Safe ATP-dependent DNase (Lucigen) at 37°C, after 3 days of digestion, heat to inactivate the exonuclease by incubating at 70°C for 30 minutes. To eliminate mitochondrial DNA, DNAs were eluted and digested with PacI (NEB) for 10 hours, and then extracted with Phenol/chloroform/isoamyl alcohol (PCI) solution (25:24:1). The ecDNA samples were extracted and the sensitivity to the exonuclease ATP-dependent DNase (Lucigen) was verified in order to determine the circular DNA samples obtained. The concentration of ecDNA in the tube was measured at 0 h, 24 h, 48 h, and 72 h. The concentration of ecDNA in the sample tubes did not change after exonuclease digestion, which proved that the circular DNA was obtained and the integrity of the loop was retained.

ecDNA linearization

ecDNA linearization was performed following the reported method of Zhang's lab(*36*). ecDNA was lineared by using the nickase fnCpf1 (NEB, M0653), 50 ng ecDNAs were nicked by incubating in a 20 μL reaction that contained 10× fnCpf1 linearization buffer and 1 μL fnCpf1 at 37 °C for 1 h, Nicked ecDNAs were linearized in 10 μL reaction that include 2 μL 5× buffer, 1 μL S1 Nuclease (Thermo Fisher, 18001016) at 37 °C for 5 min.The successful linearization of ecDNA was verified by verifying its sensitivity to exonucleaseATP-dependent DNase (Lucigen). After treatment with exonuclease, The concentration decreased in a time-dependent manner, indicating that the sample was already linear.

Assay of DNase1L3 activity for degrading ecDNA in vitro

Proteins were diluted immediately before use to a final concentration of 10 mg/mL and various combinations and concentrations of cations. Purified ecDNA or linear DNA were co-incubation with DNase1L3 protein in a solution containing 5 mM $MgCl_2$, 2.5 mM $CaCl_2$ at 37 °C for 1 h. $ZnCl_2$ was added to the reaction to inhibit the nuclease activity of DNase1L3. When conducting the liposome containing reaction, ecDNA was pre-incubated with liposomes for 10 min at room temperature, then proteins were added, pipe gently and incubate the reaction at 37 °C for 30 min or 2 h. The DNA concentration was measured by Qubit.

Immunofluorescence staining

Cells were cultured on coverslips in 24-well plates, and then were washed three times with PBS, fixed with 4% paraformaldehyde for 20 minutes and permeabilized with blocking buffer (QuickBlock Blocking Buffer for Immunol Staining, Beyotime) for 30 minutes at room

temperature. Subsequently, the cells were incubated with primary antibodies for 2 hours at room temperature. The cells were washed with PBS (3×5 minutes) and incubated with fluorochrome-labeled secondary antibody for 2 hours and phalloidin-594 for 30 minutes at room temperature. Finally, coverslips were stained with DAPI and the analysis of immunofluorescence using ZEISS LSM 800 Inverted Confocal microscope attached with an Airyscan area detector.

BODIPY staining of lipid droplets

Cells were co-incubated in PBS containing Hoechst and 20 μg/mL BODIPY-558/568 for 45 min at 37°C, and then were washed three times with PBS. For fluorescence imaging, cells were visualized using live imaging by SIM. For lipid droplets in fixed samples, cells were stained with 1 μg/mL BODIPY-493/503 and DAPI for 10 min at room temperature, and then visualized using SIM.

Scanning electron microscope (SEM)

Soak the sample with 2.5% glutaraldehyde, overnight at 4°C, dehydration with gradient ethanol twice, 15 minutes each time. Gradient tert-butanol was dried for 15 minutes each time, after which the sample was condensed at four degrees and dried in vacuum. Spray gold, the sample was imaged with scanning electron microscope.

Duolink in situ proximity ligation assay (PLA)

The Duolink in situ PLA was performed using Duolink In Situ Red Starter Kit Mouse/Rabbit (Sigma-Aldrich) according to the manufacturer's protocol. In brief, PLC-PRF-5 cells were plated on glass coverslips, rinsed three times with PBS and fixed in 4% formaldehyde in PBS for 10 minutes. The cells were permeabilized in 0.5% TritonX-100 for 5 minutes and blocked with 3% BSA in PBS for 60 minutes at 37°C. After blocking, cells were then incubated with primary antibodies in PBS containing 1% BSA overnight at 4°C, followed by incubation with corresponding secondary antibodies conjugated with PLA probes for 60 minutes at 37°C in the dark. Cells were washed three times in wash buffer. Finally, the cells were stained with DAPI, and Duolink signals were detected using ZEISS LSM 800 Inverted Confocal microscope attached with an Airyscan area detector.

Metaphase chromosome spread

After 2 hours treatment with 0.1 μg/mL colchicine, cells in metaphase were obtained. Cells were collected, washed with PBS, and suspended in 0.075 M KCl for 15-30 minutes. Carnoy's fixative (3:1, methanol: glacial acetic acid) were added to stop the reaction. The cells were washed additional 3 times with Carnoy's fixative, and then dropped on a moistened glass coverslip. DAPI

was added to the slides for ecSeg analysis. Images were acquired on the ZEISS LSM 800 Inverted Confocal microscope attached with an Airyscan area detector.

DNA FISH for cells

FISH was performed by applying Cell specimen FISH pretreatment kit (EXONBIO, Guangzhou, D-0014). In brief, FISH was performed by adding 10 μL DNA FISH probes (EXONBIO, Guangzhou) onto slides containing fixed cells in interphase or metaphase, followed by applying a coverslip and seal with rubber cement. DNA denaturation was performed at 85°C for 5 minutes, then hybridization in the hybridizer overnight at 42°C. Wash the slides in 1×wash buffer for 2 minutes at 72°C, followed by a final wash in 1×wash buffer at room temperature for 5 minutes. Metaphase cells and interphase nuclei were stained with DAPI, a coverslip was applied and images were captured on the ZEISS LSM 800 Inverted Confocal microscope attached with an Airyscan area detector.

DNA FISH for tissues

FISH was performed by applying Paraffin Pretreatment Kit (EXONBIO, Guangzhou, D-0002). In brief, specimens were baked at 70°C for more than 2 hours and then immersed in xylene substitute for dewaxing. Subsequently, soak the specimens in 100% alcohol for dehydration and air dry. Put the slices into the boiled pretreatment solution (100 ± 5°C) for 25 minutes. Soak in PBS for 2×5 minutes. Followed by protein digestion process at 37°C for 20 minutes, wash in PBS for 2×5 minutes. Dehydration step was performed in 75%, 85% and 100% alcohol for 1 minute each. DNA FISH was performed as described previously and images were captured on the ZEISS LSM 800 Inverted Confocal microscope attached with an Airyscan area detector.

Immunofluorescence combined with DNA FISH

Immunofluorescence was performed as previously described. After incubating the cells with the secondary antibodies, cells were washed three times in PBS for 5 min at RT and fixed with 4% PFA in PBS for 10 minutes, washed three times in PBS. Cells were incubated in 70% ethanol, 85% ethanol and then 100% ethanol for 1 minutes at RT. 10 μL of probe hybridization mixture was added on a slide and coverslip was placed on top. The following steps of DNA FISH were as previously described and images were acquired on the ZEISS LSM 800 Inverted Confocal microscope attached with an Airyscan area detector.

Live-cell-imaging microscopy

To monitor DNase1L3 and lipid droplets dynamics within the cells, we transiently expressed DNase1L3-EGFP, DNase1L3$^{\Delta NT}$-EGFP, DNase1L3$^{3\times NT}$-EGFP, and GC-DNase-EGFP for 48 h

and co-stained the cells with Hoechst and 20 μg/mL BODIPY-558/568 for 45 min followed by washing 3 times in PBS, and then performed imaging experiments. Cells were imaged at the Structured light illumination microscope pre-stabilized at 37°C for 2 hours. We illuminated the sample with 488-nm laser, 561-nm laser and 405-nm laser 60× Oil lens, Z-stack images were acquired with a 0.3 μm z-step size with 3 second intervals between each volumetric imaging. For DNase1L3 and lipid droplets colocalization analysis, a straight line was drawn across the center of the objects in a 2D plane and the fluorescent intensity was profiled along the line path.

Immunohistochemical (IHC) staining

The tissue samples were dissected in PBS, the tissues were fixed overnight in 4% formalin, embedded in paraffin, 4 μm sectioned, and stained with hematoxylin and eosin (H&E) for pathological examination. Tissue slides were deparaffinized in xylene and rehydrated in a graded series of ethanol. The slides were immersed in sodium citrate buffer and boiled for 25 minutes for antigen retrieval. After blocking endogenous peroxidase activity with 0.3% hydrogen peroxide and blocking nonspecific protein binding with goat serum. Incubate the section with the primary antibody overnight at 4°C. Next, incubate the section with the peroxidase-conjugated secondary antibody, rinse with PBS Three times for 5 minutes each, add DAB solution dropwise for 6 minutes, and terminate in water color rendering. Tissue slides are photographed to obtain images. Images were performed for IHC scoring, to be specific, the degree of staining (0-3 points) and the rate of positivity (0-4 points) in the immunohistochemical sections were scored separately and multiplied to obtain a comprehensive score (0-12 points). The staining intensity was scored as follows: 0 for no staining, 1 for light yellow, 2 for brownish yellow, and 3 for brownish brown; 0-5% was scored as 0, 6%-25% as 1, 26%-50% as 2, 51%-75% as 3, and 75% as 4.

RNA-seq

Total RNA was extracted by RNeasy mini kit (Qiagen) for sequencing with TruSeq RNA Library Prep Kit v2 (Illumina) according to the manufacturer's instruction. In brief, total RNA was firstly processed with poly-A selection and fragmentation, and then first-and second-strand cDNA was synthesized and ligated with sequencing adaptor. The library was finally sequenced in high throughput on the Illumina Hiseq platform in 2×150 bp pair-end sequencing mode to obtain FastQ data. Data were processed following the TCGA mRNA analysis pipeline. Expression level of mRNA was computed as FPKM for cell line samples and TCGA samples.

Circle-Seq library preparation and sequencing

EcDNA sequencing Service was provided by Shanghai Jiayin Biotechnology (Shanghai, China) by following the published procedures (10.1038/protex.2019.006). In brief, MagAttract HMW DNA Kit (Qiagen, Hilden, Germany, 67563) was applied for genomic DNA extraction. To eliminate linear chromosomal DNA and purify circular DNA, the genomic DNA was treated with Plasmid-Safe ATP-dependent DNase (Lucigen) at 37°C, after 6 days of digestion, heat inactivate the exonuclease by incubating at 70°C for 30 minutes and then extracted with Phenol/chloroform/isoamyl alcohol (PCI) solution (25:24:1). To confirm elimination of linear chromosomal DNA, quantitative PCR of HBB gene was performed. Amplify the remaining circular DNA in the reaction by MDA using φ29 DNA polymerase and random hexamer primers (REPLI-g Mini Kit (Qiagen, Hilden, Germany, 150025)), followed by sample clean up (Agencourt AMPure XP magnetic beads (Beckman Coulter, Brea, CA, USA, A63880)). The samples were used for DNA Library Preparation and Next Generation Paired-End Sequencing using Illumina MiSeq Technology. ecDNA larger than 10kb was screened for subsequent analysis.

ecDNA identification from Circle-Seq data

We applied Circle-Map software to detect ecDNA from sequencing data. Firstly, sequencing reads were aligned to the human reference genome (hg38 genome download from UCSC) using BWA-MEM(RRID:SCR_017619). Then, to detect the coordinates of each ecDNA, two BAM files which were sorted according to read names and coordinates for the extraction of circular reads were used. Several filtering steps were conducted to improve the accuracy of ecDNA detection. The specific settings were as follows: (1) split reads ≥ 2, (2) circle score ≥ 20, (3) coverage increase in the start coordinate ≥ .33, (4) coverage increase in the end coordinate ≥ .33, (5) coverage continuity ≤ .1 and (6) The SD of coverage smaller than the mean coverage over the whole ecDNA region.

Molecular Dynamics Simulations

Vitamin D binding protein was downloaded from RCSB PDB data bank (http://www.rcsb.org, PDB ID:1J78, RRID:SCR_012820). After obtaining the 3D structures of the protein and Vitamin D molecular, the molecular docking process was performed with Rosetta8. Based on a maximum number of 100 conformers extracted from precise docking, we obtained the final conformer owing the lowest binding energy.

For simulations of the protein and aptamer systems, the AMBER FF14SB and AMBER PARM99 force fields were used respectively. Each system (the protein−protein complex) was solvated in TIP3P water and NaCl to neutralize the systems. All-atom MD simulations were carried out by using the GROMACS 2019.03 package. The systems were restrained by a harmonic potential of

the form k (Δx)2 where the force constant k was 100 kcal/mol-1Å-2. Then, we optimized the water molecules and counter ions using the steepest descent and conjugate gradient for 2500 steps separately. After that, we optimized the entire systems without any constraint using the first step method, following by an annealing simulation process under a weak restraint (k=100 kcal/mol-1Å-2). The complex systems were heated from 0 to 298 K gradually over 500 ps in the NVT ensemble (i.e., N represents the number of particles, V represents the volume and T represents the temperature of the systems, and their product was a constant). After this heating phase, we performed a 40 ns MD simulation under 1 atm with a constant temperature at 298 K and a constant pressure maintained by isotropic position scaling algorithm with a relaxation time of 2 ps.

Animal studies

Animal experiments were carried out in accordance with the National Institutes of Health Animal Use Guidelines. All of the experimental protocols have been approved by the Institutional Animal Care and Use Committee.

In vivo orthotopic implantation models: Female BALB/c mice aged 4–6 weeks were used in the experiments. In brief, 1×10^6 H22-luc cells, or H22-Luc cells transfected with plasmid of DNase1L3-pcDNA3.1+/C-(K)-DYK, DNase1L3$^{\Delta NT}$-pcDNA3.1+/C-(K)-DYK, DNase1L3$^{3\times NT}$-pcDNA3.1+/C-(K)-DYK, GC-pcDNA3.1+/C-(K)-DYK, DNASE1L3 ko_eSpCas9-2A-Puro(PX459)V2.0, ko GC_eSpCas9-2A- Puro (PX459)V2.0 were suspended in 100 μL of Sanitary saline respectively and injected orthotopically into the left liver lobe of BALB/c mice. Tumor growth was detected in vivo after injection of 150 mg/kg D-Luciferin and potassium salt substrate (Yeasen, CN) in PBS into anesthetized mice with NightOWLIILB983 (Berthold Technologies). The mice were killed and the liver were preserved in 10% formalin solution for further study. For VD treatment experiments, mice transplanted with H22-luc cells were randomly divided into three groups, which were control group, VD low-dose group and VD high-dose group. mice in the control group had anhydrous ethanol added to their daily drinking water, and in the VD low-dose group, anhydrous ethanol-dissolved VD3, 600 IU/kg was added to their daily drinking water. in the VD high-dose group, anhydrous ethanol-dissolved VD3, 1500 IU/kg was added to their daily drinking water. the drug was administered continuously for 2 months. For other experiments involving VD administration, VD was treated in the same way and at the same dose as the VD high-dose group, while the other groups of mice were given anhydrous ethanol as a control.

Diethylnitrosamine (DEN)-induced mouse models: 2-week-old C57BL/6 mice were given a single intraperitoneal injection of DEN (25 mg/kg body weight). After one week, the DEN-

challenged mice were given Carbon tetrachloride (0.5 mg/kg body weight) by intraperitoneal injections once a week for 5 months. Mice were randomly divided into two groups of 6 mice each. The mice in the experimental group were injected with 1×10^{11} virus particles of AAV8-encapsulated ko DNase1L3 plasmid in 200 μL PBS in the tail vein, followed by two booster injections at an interval of less than 1 week, the control mice were injected with 200 μL PBS in the tail vein. After 10 months, the livers of mice were analyzed for number and size of hepatic tumors.

PDX mouse models: 8 fresh surgical tumor tissues (F0, hepatocellular carcinoma) were collected immediately after surgery without any other treatment from 8 patients in Tianjin Medical University Cancer Institute and Hospital. The information of the patients is provided in tableS2. A written informed consent was obtained from each patient. According to the Declaration of Helsinki, studies were performed after approval of the ethics committee of Nankai University, including the use of animal experiments and tumor specimens. Tumor fragments were implanted subcutaneously into the right axilla of 4-6 week-old BALB/c nude mice. By palpation of the skin at the tumor site, we selected mice that bore tumor nodules and began to measure the tumor volumes. When the tumor size reached 100 to 200 mm^3, the samples (F1) were divided into pieces for in vivo passaging to construct F2 and then F3 tumors as described above. When the F3 tumor size reached 100 to 200 mm^3, the mice bearing different tumor types were randomly divided into control, DNase1L3 mRNA and GC-DNase mRNA groups consisting of eight mice per group. mRNA of DNase1L3 and GC-DNase were synthesized by GenScript, LNP encapsulation of mRNA is performed by Nuohai Life Science (Shanghai) Co, LTd. 100 μL LNP containing 3 μg mRNA was injected intravenously to BALB/c nude mice every 5 days for 10 times. Mice in the control group were injected intravenously with 100 μL LNP solution.

Bioinformatics analysis

The clinical information and gene expression data of hepatocellular carcinoma in The Cancer Genome Atlas (TCGA) were downloaded using the R package “TCGAbiolinks” and analyzed by the R package “ggplot2”, “survival” and “survminer”. Gene set enrichment analysis (GSEA, RRID:SCR_003199) was carried out using R package “clusterProfiler”.

Statistical analysis

Statistical analyses were performed using GraphPad Prism version 9 for Windows or R 4.1.3. Statistically significant differences were calculated using two-tailed unpaired t-tests, or unpaired t test with Welch's correction, Pearson’s correlation, and Kaplan–Meier as needed. $P<0.05$ was

considered significant. For fluorescence intensity statistics, measurements were made using the Profile and Measure functions of the ZEN Blue software. For the number and area statistics of fluorescent signal points, as well as the statistics of wound healing area and number of colony were measured using the Analyze Particles function of ImageJ software. For the analysis of overlapping signals of two channels, after importing the original image using ImageJ software and splitting it by channel, selecting the Min algorithm in the image calculation module, following by selecting the images of the two channels to be analyzed, confirming and generating the images of the two overlapping channels, and then measuring the overall intensity.

Materials Table

REAGENT or RESOURCE	SOURCE	IDENTIFIER
Antibodies		
Mouse monoclonal anti-Vimentin	Proteintech	Cat# 60330-1-Ig; RRID: AB_2881439
Mouse monoclonal anti-ZEB1	Proteintech	Cat#66279-1-Ig; RRID: AB_2881662
Rabbit polyclonal anti-Twist1	Proteintech	Cat# 25465-1-AP; RRID: AB_2880093
Rat monoclonal anti-CD324 (E-Cadherin)	Invitrogen	Cat# 53-3249-80; RRID: AB_10671270
Rabbit polyclonal anti-beta Actin	Affinity	Cat# AF7018; RRID: AB_2839420
Mouse monoclonal anti-Vitamin D binding protein (DBP)	Proteintech	Cat# 66175-1-Ig; RRID: AB_2881570
Mouse monoclonal anti-DNasel3	Proteintech	Cat# 67041-1-Ig; RRID: AB_2882355
Rabbit polyclonal anti-Histone-H3	Proteintech	Cat# 17168-1-AP; RRID: AB_2716755
Rabbit polyclonal anti-ubiquitin	Proteintech	Cat# 10201-2-AP; RRID: AB_671515
Rabbit polyclonal anti-USP25	Proteintech	Cat# 12199-1-AP; RRID: AB_2212771
Rabbit polyclonal anti-DYKDDDDK tag	Proteintech	Cat# 20543-1-AP; RRID: AB_11232216
Rabbit polyclonal anti-BRAF	Proteintech	Cat# 20899-1-AP; RRID: AB_2882047
Rabbit polyclonal anti-KRAS	Proteintech	Cat# 12063-1-AP
Rabbit polyclonal anti-SRPK1	Proteintech	Cat# 14073-1-AP; RRID: AB_2194745
Rabbit polyclonal anti-CENPF	Proteintech	Cat# 28568-1-AP; RRID: AB_2918176
Rabbit monoclonal anti-PARP1	ZENBIO	Cat# R25279;
Mouse monoclonal anti-ADFP	ZENBIO	Cat# 220889;
Mouse monoclonal anti-PADPr	Santa Cruz	Cat# sc-56198; RRID: AB_785249
YF 633-Phalloidin	US Everbright	Cat# YP0053S;
YF 647 Goat Anti-Rabbit IgG (H&L)	US Everbright	Cat# Y6109L;
CoraLite 488-conjugated Goat Anti-Mouse IgG(H+L)	Proteintech	Cat# SA00013-1; RRID: AB_2810983

Goat Anti-Rabbit IgG (H+L) HRP	Affinity	Cat# S0001; RRID: AB_2839429
Goat Anti-Mouse IgG (H+L) HRP	Affinity	Cat# S0002; RRID: AB_2839430
Biological samples		
HCC samples for patient-derived xenografts	Tianjin Medical University Cancer Institute and Hospital	N/A
Chemicals, peptides, and recombinant proteins		
Cycloheximide (CHX)	Solomen	CAT# IN0194; CAS: 66-81-9
Forskolin	Meilunbio	CAT# MB5959; CAS: 66575-29-9
MG132	Med Chem Express	CAT# HY-13259C CAS: 1211877-36-9
Oleic acid	HEOWNS	CAT# 0443469; CAS: 112-80-1
25-hydroxy Vitamin D3	Med Chem Express	CAT# HY-32351; CAS: 19356-17-3
1,25-Dihydroxyvitamin D3	Med Chem Express	CAT# HY-10002; CAS: 32222-06-3
VD3	Med Chem Express	CAT# HY-15398 CAS: 67-97-0
Colchicine	MERYER	CAT# M22777; CAS: 64-86-8
PEI 25K	Polysciences	CAT# 23966100; CAS: 9002-98-6
DYKDDDDK Peptide	GenScript	CAT# RP10586
Plasmid-Safe ATP-Dependent DNase	Biosearch Technologies	CAT# E3101K
EnGen Lba Cas12a (Cpf1)	New England Biolabs	CAT# M0653S
S1 Nuclease	ThermoFisher	CAT# 18001-016
SYBR Gold nucleic acid gel stain	ThermoFisher	CAT# S11494
GeneRuler 1kb Plus DNA Ladder	ThermoFisher	CAT# SM1331
Color-enhanced prestained protein molecular weight markers (10-245kD)	SparkJade	CAT# EC0020
BODIPY 493/503	GlpBio	CAT# GC42959; CAS: 121207-31-6
BODIPY 558/568	Cayman Chemical	CAT# 27014 CAS: 158757-84-7
Salidroside	Meilunbio	CAT# MB5843-1; CAS: 10338-51-9
Artemisinin	TCI chemicals	CAT# A2118; CAS: 63968-64-9
Myricetin	Med Chem Express	CAT# HY-15097; CAS: 529-44-2
Hesperetin	PUSH BIOTechnology	CAT# PS0243; CAS: 520-33-2
Baicalein	PUSH BIOTechnology	CAT# PS0711 CAS: 491-67-8
Puerarin	PUSH BIOTechnology	CAT# PS0180; CAS: 3681-99-0
Vitamin C	PUSH BIOTechnology	CAT# PS2289 CAS: 50-81-7
Lentinan	Aladdin	CAT# L413225; CAS: 37339-90-5

Sodium butyrate	Aladdin	CAT# S102956 CAS: 156-54-7
Metformin	MACKLIN	CAT# N886063; CAS: 657-24-9
Critical commercial assays		
Cell Counting Kit-8 (CCK-8)	APExBIO	CAT# K1018
DNA Native PAGE Electrophoresis Kit	RealTimes	CAT# RTE4101
One-4-All Genomic DNA Miniprep Kit	BIO BASIC	CAT# B618503
Lipid Droplet Isolation Kit	CELL BIOLABS	CAT# MET-5011
Cell Specimen FISH Pretreatment Kit	Exon Biological	CAT# D-0014
Paraffin Pretreatment Kit II	Exon Biological	CAT# D-0002
Fast Silver Stain Kit	Beyotime	CAT# P0017S
Duolink In Situ Detection Reagents Orange	Sigma Aldrich	CAT# DUO92007
Duolink In Situ PLA Probe Anti-Rabbit MINUS	Sigma Aldrich	CAT# DUO92005
Duolink In Situ PLA Probe Anti-Mouse PLUS	Sigma Aldrich	CAT# DUO92001
MonoRab Anti-DYKDDDDK Magnetic Beads	GenScript	CAT# L00835
MagAttract HMW DNA Kit	QIAGEN	CAT# 67563
Experimental models: Cell lines		
Hep3B	CELLCOOK	CAT#CC0103
SK-Hep1	Keygen Biotech	CAT#KG064
PLC-PRF-5	Keygen Biotech	CAT#KG068
H22-LUC	ZQXZbio	CAT# LZQ0029
MHCC-97L	ZQXZbio	CAT# ZQ0019
MHCC-97H	ZQXZbio	CAT# ZQ 0020
Experimental models: Organisms/strains		
BALB/c mice	Beijing Vital River Laboratory Animal Technology	
C57BL/6 mice	Beijing Vital River Laboratory Animal Technology	
BALB/c nude mice	Beijing Vital River Laboratory Animal Technology	
Oligonucleotides		
Primers for DNase1L3 Forward: TGCAGCTACGTCCCCAAGA Reverse: TCCCCGATCAGCCAAACAAAC	TsingkeBiotechnology	
Primers for GAPDH Forward: ACAACTTTGGTATCGTGGAAGG Reverse: GCCATCACGCCACAGTTTC	TsingkeBiotechnology	
Primers for BRAF mRNA Forward: AATACACCAGCAAGCTAGATGC Reverse: AATCAGTTCCGTTCCCCAGAG	TsingkeBiotechnology	
Primers for KRAS mRNA Forward: ACAGAGAGTGGAGGATGCTTT Reverse: TTTCACACAGCCAGGAGTCTT	TsingkeBiotechnology	
Primers for SRPK1 mRNA Forward: CCATGTGATCCGAAAGTTAGGC Reverse: AGGGTCTGAATTGCGAACTGA	TsingkeBiotechnology	

Primers for BRAF ecDNA forward: TTTTCTGTCTTCTTCCTCTGTGT Reverse: TCAATGTATGTTCTTGGCACCT	TsingkeBiotechnology	
Primers for KRAS ecDNA forward: AAGAGTTTGGAGTTGGAATTGC Reverse: GCCTCTGCCTACTTGTCTCC	TsingkeBiotechnology	
Primers for SRPK1 ecDNA forward: GTCTGCTGGGGTAGGTAGTC Reverse: TTCTCTGCTCTCGAACCCTG	TsingkeBiotechnology	
Recombinant DNA		
GC_OHu14110D_pcDNA3.1+/C-(K)-DYK	Genscript	
DNASE1L3_OHu20141D_pcDNA3.1+/C-(K)-DYK	Genscript	
DNase1L3$^{\Delta NT}$-mEGFP	TsingkeBiotechnology	
DNase1L3$^{3\times NT}$-EGFP	TsingkeBiotechnology	
DNase1L3-EGFP	TsingkeBiotechnology	
GC-DNase-mEGFP	TsingkeBiotechnology	
GC-EGFP	TsingkeBiotechnology	
NLS-GC_pcDNA3.1+/C-(K)-DYK	TsingkeBiotechnology	
NES-GC_pcDNA3.1+/C-(K)-DYK	TsingkeBiotechnology	
CRISPR/Cas9-based knock out		Targeting Sequence (5'-3')
sgRNA: Ko VDR_eSpCas9-2A-Puro (PX459) V2.0	Genscript	ACTTTGACCGGAACGTGCCC
sgRNA: ko GC_eSpCas9-2A- Puro (PX459) V2.0	Genscript	ACCCTGACTGCTATGACACC
sgRNA: DNase1L3 ko_eSpCas9-2A- Puro (PX459) V2.0	Genscript	CTGTGACATCATACTCGTGA
sgRNA: Ko USP25_eSpCas9-2A-Puro (PX459) V2.0	Genscript	GTTGATTCAAAAACGTCTGC
sgRNA: KRAS ko_eSpCas9-2A- Puro (PX459) V2.0	Genscript	AAATATAGATGAAGGTACTA
sgRNA: BRAF ko_eSpCas9-2A- Puro (PX459) V2.0	Genscript	TTCTTGGCACCTTCATAATG
sgRNA: SRPK1 ko_eSpCas9-2A- Puro (PX459) V2.0	Genscript	CTCATCACTCCCCATCTCAT
DNA FISH probes Targeted Gene	Coordinates of the FISH probes	BAC ID
BRAF	Chr7:140503484-140699716	RP11-948O19
KRAS	Chr12:25230469-25426524	RP11-295I5
SRPK1	Chr6:35799497—35955913	RP11-122J19

959

Software and algorithms			
ZEN	Zeiss		https://www.zeiss.com/microscopy/en/products/software/zeiss-zen.html
Ecseg	https://doi.org/10.1016/j.isci.2019.10.035.		https://github.com/UCRajkumar/ecSeg
Circle-Map	https://doi.org/10.1186/s12859-019-3160-3		https://github.com/iprada/Circle-Map
IGV	IGV		https://igv.org/
R 4.1.3	R Foundation	RRID:SCR_001905	https://www.r-project.org/

ImageJ	Open source processing software	RRID:SCR_003070	https://imagej.nih.gov/ij/
GraphPad Prism 9.0.0	GraphPad	RRID:SCR_002798	https://www.graphpad.com/scientific-software/prism/
FlowJo 10.6.2 Software	FlowJo LLC	RRID:SCR_008520	https://www.flowjo.com/
Pymol	Schrödinger, LLC	RRID:SCR_000305	https://pymol.org/2/
GROMACS	GROMACS	RRID:SCR_014565	https://www.gromacs.org/
Other			
Zeiss LSM800 with Airyscan	Zeiss		
Zeiss Elyra7	Zeiss		
mRNA Drugs			
Name	Vector	DNA template	
DNase1L3	pUC57-mini-Kana-BsmBI free-terminator-T7 deleted-100A-BspQI	AAGCTTTAATACGACTCACTATAAGGGGCTAGCGATCTTCTGGTCCCCACAGACTCAGAGAGAACCCGCCACCATGTCTCGTGAGCTGGCCCCTTTGCTACTCCTGCTGTTGAGCATCCATTCTGCATTGGCCATGCGGATCTGTTCCTTTAATGTGCGTTCATTTGGAGAGTCTAAGCAGGAAGACAAAAATGCAATGGATGTCATTGTCAAAGTCATTAAAAGATGTGACATAATTCTTGTGATGGAGATCAAGGACTCTAACAACAGGATATGCCCCATTTTAATGGAAAAGCTCAATAGAAACTCAAGACGAGGCATCACCTACAACTACGTGATTAGTTCACGGCTCGGGAGAAATACCTATAAGGAGCAGTATGCTTTCCTGTATAAAGAGAAACTGGTGTCTGTGAAACGGTCCTACCACTACCATGACTACCAGGATGGAGATGCTGATGTATTCTCCCGAGAACCCTTCGTGGTCTGGTTCCAGTCTCCTCACACAGCTGTGAAGGATTTTGTCATCATCCCGCTGCACACGACACCTGAAACCAGCGTTAAAGAAATTGATGAGTTAGTGGAGGTCTACACAGATGTGAAGCACCGCTGGAAAGCAGAGAACTTCATCTTCATGGGTGACTTCAACGCAGGCTGCAGCTATGTTCCCAAGAAAGCCTGGAAGAACATCCGGCTCAGAACTGACCCAAGGTTTGTGTGGCTGATAGGGGACCAAGAAGACACTACTGTTAAAAAGTCCACGAACTGCGCCTATGATCGCATCGTACTACGCGGCCAGGAGATTGTTAGCAGCGTGGTGCCAAAAAGCAATAGTGTGTTTGACTTTCAGAAGGCCTACAAGCTGACCGAAGAGGAAGCTCTGGATGTATCGGACCATTTCCCAGTAGAGTTTAAGCTGCAATCCTCTAGGGCGTTCACAAATAGCAAGAAGTCAGTCACCCTTAGGAAGAAGACCAAGAGTAAAAGGTCCTGATAATAGGCTGGAGCCTCGGTGGCCATGCTTCTTGCCCCTTGGGCCTCCCCCCAGCCCCTCCTCCCCTTCCTGCACCCGTACCCCCGTGGTCTTTGAATAAAGTCTGAGTGGGCGGCAGGATCCCGTCTCTTAACTAACTAAACTAGTAAAAA

GC -Dnase	pUC57-mini-Kana-BsmBI free-terminator-T7 deleted-100A-BspQI	AAGCTTTAATACGACTCACTATAAGGGGCTAGCGATCTTCTGGTCCCCA CAGACTCAGAGAGAACCCGCCACCATGAAGAGAGTGTTGGTGTTACTG TTGGCAGTGGCATTTGGACACGCCCTGGAGCGAGGCAGAGATTACGAG AAGAACAAAGTATGTAAAGAGTTTAGTCACCTTGGGAAGGAAGACTTT ACCAGCCTCAGCCTGGTTCTGTACAGCAGGAAGTTCCCCAGTGGGACGT TTGAACAAGTGTCCCAACTGGTCAAGGAGGTGGTTTCTCTGACAGAAGC CTGTTGTGCCGAAGGCGCCGACCCGGACTGTTATGACACGAGAACTTCA GCCCTGTCCGCAAAATCCTGCGAGAGCAATTCCCCCTTTCCTGTGCATC CCGGGACCGCAGAATGTTGCACCAAAGAAGGGCTCGAACGCAAATTAT GTATGGCAGCTCTAAAACACCAGCCTCAGGAATTCCCGACATATGTCGA GCCCACCAATGACGAGATCTGTGAGGCCTTCCGGAAAGACCCTAAGGA GTATGCCAACCAGTTCATGTGGGAGTACTCCACTAACTATGGGCAGGCT CCGCTCTCACTTCTGGTATCATACACGAAGAGTTACCTCTCCATGGTCG GGAGCTGCTGCACAAGCGCCAGCCCTACCGTTTGTTTTCTTAAAGAAAG ACTGCAGCTCAAACATCTCTCCCTCCTGACTACTCTGAGTAACCGGGTG TGCTCCCAGTATGCAGCGTATGGAGAAAAGAAGTCTAGGCTTTCCAATC TGATCAAACTAGCTCAAAAGGTTCCCACGGCTGACCTCGAAGATGTCCT TCCATTGGCAGAAGACATCACAAACATTCTCTCTAAGTGTTGTGAGTCC GCGAGTGAAGATTGCATGGCCAAAGAATTACCAGAGCACACCGTGAAA CTATGCGACAACCTCTCTACCAAAAATTCGAAATTCGAGGACTGCTGCC AGGAGAAAACTGCGATGGACGTATTTGTCTGCACATATTTTATGCCTGC TGCCCAGCTGCCCGAACTCCCAGACGTGGAACTTCCAACTAACAAGGAC GTCTGTGACCCAGGTAACACTAAGGTCATGGATAAGTACACCTTCGAGC TCAGCAGGAGGACTCATCTCCCAGAAGTTTTCCTTAGCAAGGTATTGGA GCCTACGCTAAAATCACTGGGCGAATGCTGTGATGTGGAGGATAGCAC AACTTGTTTCAATGCTAAGGGCCCTCTGCTCAAGAAGGAGTTGTCGAGC TTCATCGACAAGGGACAAGAGCTGTGCGCCGACTACAGTGAGAATACT TTCACTGAGTATAAGAAAAAGCTGGCCGAGCGATTGAAGGCTTGATAAT AGGCTGGAGCCTCGGTGGCCATGCTTCTTGCCCCTTGGGCCTCCCCCCA GCCCCTCCTCCCCTTCCTGCACCCGTACCCCCGTGGTCTTTGAATAAAGT CTGAGTGGGCGGCAGGATCCCGTCTCTTAACTAACTAAACTAGTAAAAA AAAAAAAAAAAAAAAAAAAAAAAAAAAAAAAAAAAAAAAAAAAAAAA AAAAAAAAAAAAAAAAAAAAAAAAAAAAAAAAAAAAAAAAAAAAAAA AAA

961

References

1. T. Paulsen, P. Kumar, M. M. Koseoglu, A. Dutta, Discoveries of Extrachromosomal Circles of DNA in Normal and Tumor Cells. *Trends Genet* **34**, 270-278 (2018).
2. K. M. Turner *et al.*, Extrachromosomal oncogene amplification drives tumour evolution and genetic heterogeneity. *Nature* **543**, 122-125 (2017).
3. S. Wu *et al.*, Circular ecDNA promotes accessible chromatin and high oncogene expression. *Nature* **575**, 699-703 (2019).
4. A. R. Morton *et al.*, Functional Enhancers Shape Extrachromosomal Oncogene Amplifications. *Cell* **179**, 1330-1341.e1313 (2019).
5. H. Kim *et al.*, Extrachromosomal DNA is associated with oncogene amplification and poor outcome across multiple cancers. *Nat Genet* **52**, 891-897 (2020).
6. E. Yi, R. Chamorro González, A. G. Henssen, R. G. W. Verhaak, Extrachromosomal DNA amplifications in cancer. *Nat Rev Genet*, (2022).
7. D. Feldman, A. V. Krishnan, S. Swami, E. Giovannucci, B. J. Feldman, The role of vitamin D in reducing cancer risk and progression. *Nature reviews. Cancer* **14**, 342-357 (2014).
8. S. Budhathoki *et al.*, Plasma 25-hydroxyvitamin D concentration and subsequent risk of total and site specific cancers in Japanese population: large case-cohort study within Japan Public Health Center-based Prospective Study cohort. *BMJ* **360**, k671 (2018).
9. P. D. Chandler *et al.*, Effect of Vitamin D3 Supplements on Development of Advanced Cancer: A Secondary Analysis of the VITAL Randomized Clinical Trial. *JAMA Netw Open* **3**, e2025850 (2020).
10. N. Keum, D. H. Lee, D. C. Greenwood, J. E. Manson, E. Giovannucci, Vitamin D supplementation and total cancer incidence and mortality: a meta-analysis of randomized controlled trials. *Ann Oncol* **30**, 733-743 (2019).
11. A. P. Fang *et al.*, Serum Bioavailable, Rather Than Total, 25-hydroxyvitamin D Levels Are Associated With Hepatocellular Carcinoma Survival. *Hepatology* **72**, 169-182 (2020).
12. U. Rajkumar *et al.*, EcSeg: Semantic Segmentation of Metaphase Images Containing Extrachromosomal DNA. *iScience* **21**, 428-435 (2019).
13. M. J. Keiser *et al.*, Relating protein pharmacology by ligand chemistry. *Nat Biotechnol* **25**, 197-206 (2007).
14. A. Daina, O. Michielin, V. Zoete, SwissTargetPrediction: updated data and new features for efficient prediction of protein targets of small molecules. *Nucleic Acids Res* **47**, W357-W364 (2019).
15. X. Liu, I. Vogt, T. Haque, M. Campillos, HitPick: a web server for hit identification and target prediction of chemical screenings. *Bioinformatics* **29**, 1910-1912 (2013).
16. C. Verboven *et al.*, A structural basis for the unique binding features of the human vitamin D-binding protein. *Nature Structural Biology* **9**, 131-136 (2002).
17. K. L. Hung *et al.*, ecDNA hubs drive cooperative intermolecular oncogene expression. *Nature* **600**, 731-736 (2021).
18. D. Shiokawa, T. Kobayashi, S. Tanuma, Involvement of DNase gamma in apoptosis associated with myogenic differentiation of C2C12 cells. *J Biol Chem* **277**, 31031-31037 (2002).
19. A. G. Yakovlev *et al.*, A role of the Ca2+/Mg2+-dependent endonuclease in apoptosis and its inhibition by Poly(ADP-ribose) polymerase. *J Biol Chem* **275**, 21302-21308 (2000).

20. Y. Wang *et al.*, eccDNAs are apoptotic products with high innate immunostimulatory activity. *Nature*, (2021).
21. I. Pérez-Núñez *et al.*, LCOR mediates interferon-independent tumor immunogenicity and responsiveness to immune-checkpoint blockade in triple-negative breast cancer. *Nat Cancer* **3**, 355-370 (2022).
22. B. Li *et al.*, DNASE1L3 inhibits proliferation, invasion and metastasis of hepatocellular carcinoma by interacting with β-catenin to promote its ubiquitin degradation pathway. *Cell Prolif*, e13273 (2022).
23. V. Sisirak *et al.*, Digestion of Chromatin in Apoptotic Cell Microparticles Prevents Autoimmunity. *Cell* **166**, 88-101 (2016).
24. Y. A. Lazebnik, S. H. Kaufmann, S. Desnoyers, G. G. Poirier, W. C. Earnshaw, Cleavage of poly(ADP-ribose) polymerase by a proteinase with properties like ICE. *Nature* **371**, 346-347 (1994).
25. N. J. Curtin, C. Szabo, Poly(ADP-ribose) polymerase inhibition: past, present and future. *Nature Reviews Drug Discovery* **19**, 711-736 (2020).
26. L. Serpas *et al.*, deletion causes aberrations in length and end-motif frequencies in plasma DNA. *Proc Natl Acad Sci U S A* **116**, 641-649 (2019).
27. J. A. Olzmann, P. Carvalho, Dynamics and functions of lipid droplets. *Nat Rev Mol Cell Biol* **20**, 137-155 (2019).
28. A. Romanauska, A. Köhler, The Inner Nuclear Membrane Is a Metabolically Active Territory that Generates Nuclear Lipid Droplets. *Cell* **174**, 700-715.e718 (2018).
29. Y. Ohsaki *et al.*, PML isoform II plays a critical role in nuclear lipid droplet formation. *J Cell Biol* **212**, 29-38 (2016).
30. K. Sołtysik *et al.*, Nuclear lipid droplets form in the inner nuclear membrane in a seipin-independent manner. *J Cell Biol* **220**, (2021).
31. K. Sołtysik, Y. Ohsaki, T. Tatematsu, J. Cheng, T. Fujimoto, Nuclear lipid droplets derive from a lipoprotein precursor and regulate phosphatidylcholine synthesis. *Nat Commun* **10**, 473 (2019).
32. R. Bouillon *et al.*, The health effects of vitamin D supplementation: evidence from human studies. *Nat Rev Endocrinol* **18**, 96-110 (2022).
33. C. Triantos, I. Aggeletopoulou, K. Thomopoulos, A. Mouzaki, Vitamin D-Liver Disease Association: Biological Basis and Mechanisms of Action. *Hepatology* **74**, 1065-1073 (2021).
34. K. Kitami *et al.*, Peritoneal restoration by repurposing vitamin D inhibits ovarian cancer dissemination via blockade of the TGF-β1/thrombospondin-1 axis. *Matrix Biol* **109**, 70-90 (2022).
35. J. Hahn *et al.*, Vitamin D and marine omega 3 fatty acid supplementation and incident autoimmune disease: VITAL randomized controlled trial. *BMJ* **376**, e066452 (2022).
36. Y. Wang *et al.*, eccDNAs are apoptotic products with high innate immunostimulatory activity. *Nature* **599**, 308-314 (2021).

Acknowledgments: We are grateful to Prof. Vineet Bafna and Prof. Jens Luebeck for valuable guidance.

Funding: This study was supported by the National Natural Science Foundation of China (grant no. 81872374, 81972629 and 81972746).

Author contributions: Heng Zhang and Lu-ning Qin carried out experiments, analyzed data, drafted the manuscript and edited figures. Qing-qing Li, Ting Wu, Lei Zhang, Kai-wen Wang, Shan-bin Cheng, Yue Shi and Yi-qian Feng carried out experiments and analyzed data. Jing-xia Han, Yi-nan Li, Zhi-yang Li and Hui-juan Liu provided technical support. Tao Sun conceived experiments, edited the manuscript, and secured funding. All authors had final approval of the submitted and published versions of the manuscript.

Competing interests: Authors declare that they have no competing interests.

Data and materials availability: All data are available in the main text or the supplementary materials.

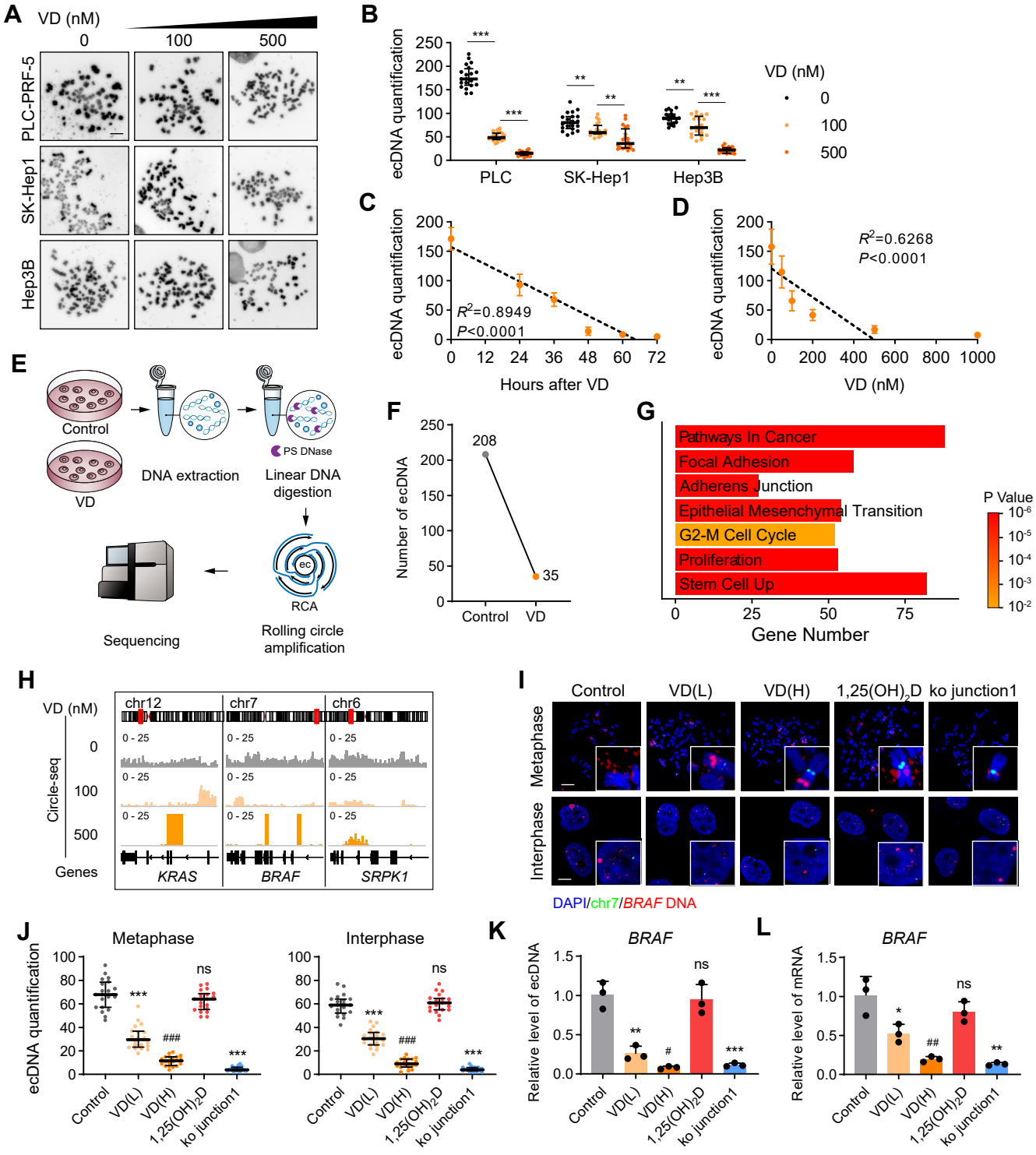
A
VD (nM)
0
100
500
PLC-PRF-5
SK-Hep1
Hep3B
B
ecDNA quantification
PLC
SK-Hep1
Hep3B
VD (nM)
0
100
500
C
ecDNA quantification
R^2=0.8949
P<0.0001
Hours after VD
D
ecDNA quantification
R^2=0.6268
P<0.0001
VD (nM)
E
Control
VD
DNA extraction
PS DNase
Linear DNA digestion
RCA
Rolling circle amplification
Sequencing
F
Number of ecDNA
208
35
Control
VD
G
Pathways In Cancer
Focal Adhesion
Adherens Junction
Epithelial Mesenchymal Transition
G2-M Cell Cycle
Proliferation
Stem Cell Up
Gene Number
P Value
H
VD (nM)
Circle-seq
Genes
chr12
chr7
chr6
KRAS
BRAF
SRPK1
I
Control
VD(L)
VD(H)
1,25(OH)2D
ko junction1
Metaphase
Interphase
DAPI/chr7/BRAF DNA
J
Metaphase
Interphase
ecDNA quantification
Control
VD(L)
VD(H)
1,25(OH)2D
ko junction1
K
BRAF
Relative level of ecDNA
L
BRAF
Relative level of mRNA

Fig. 1. VD reduced ecDNA level in HCC cells. (A and B) Representative images (**A**) and quantification (**B**) of metaphase ecDNA by ecSeg in HCC cells after treatment of DMSO or 25OHD (100 nM or 500 nM) for 48 h. Scale bar, 10 µm. 20 metaphase spreads from 3 biologically independent samples were counted. Statistics were calculated on biological replicates with unpaired *t*-test with Welch's correction. $^{**}P < 0.01$, $^{***}P < 0.001$. Error bars show median, upper and lower quartiles. **(C)** Quantification of metaphase ecDNA by ecSeg in HCC cells after treated with DMSO or 25OHD (500 nM) for indicated time points. 20 metaphase spreads from 3 biologically independent samples were counted. Statistics were calculated on biological replicates with simple linear regression. **(D)** Quantification of metaphase ecDNA by ecSeg in HCC cells after treated with different concentrations of 25OHD for 48 h. 20 metaphase spreads from 3 biologically independent samples were counted. Statistics were calculated on biological replicates with simple linear regression. **(E)** Schematic diagram of isolation, purification and sequencing of ecDNA. **(F)** The number of ecDNAs larger than 10kb was filtered from the circle-seq data in DMSO (48 h) group and 25OHD (500 nM,48 h) treatment group in PLC-PRF-5 cells of E. **(G)** Gene annotation and GO analysis of the down-regulated ecDNA in the 25OHD (500 nM, 48 h) treatment group compared to the control group (DMSO). **(H)** Circle-seq peaks at three genes (*BRAF*, *KRAS*, *SRPK1*) after treatment with different concentrations of 25OHD (0,100nM,500nM) for 48 h in PLC-PRF-5 cells. **(I)** Representative *BRAF* FISH images of metaphase ecDNA (top) and interphase ecDNA (bottom) signal in PLC-PRF-5 cells after treatment of DMSO, VD(L) (100 nM), VD(H) (500 nM), 1,25$(OH)_2$D (500 nM) or transfected with specifically ko ecDNA junction of *BRAF* plasmid for 48 h. Scale bar, 10 µm. **(J)** FISH signal quantification by ecSeg. Scale bar, 10 µm. 20 metaphase spreads or interphase cells of FISH images from 3 biologically independent samples were counted. Statistics were calculated on biological replicates with unpaired *t*-test with Welch's correction. $^{***}P < 0.001$, ns, not significant. Error bars show median, upper and lower quartiles. **(K)** QPCR detected of ecDNA levels of *BRAF* purified and isolated from PLC-PRF-5 cells treated with DMSO, VD(L) (100 nM), VD(H) (500 nM), 1,25$(OH)_2$D (500 nM) or transfected with specifically ko ecDNA junction of *BRAF* plasmid for 48 h. n=3, biological replicates. Statistics were calculated on biological replicates with two-tailed unpaired t-tests. $^{***}P < 0.001$, ns, not significant. Error bars show mean with SD. **(L)** Quantification of mRNA level of *BRAF* by qPCR in PLC-PRF-5 cells. Student's *t*-test, n=3, biological replicates. Statistics were calculated on biological replicates with two-tailed unpaired t-tests. $^{***}P < 0.001$, ns, not significant. Error bars show mean with SD.

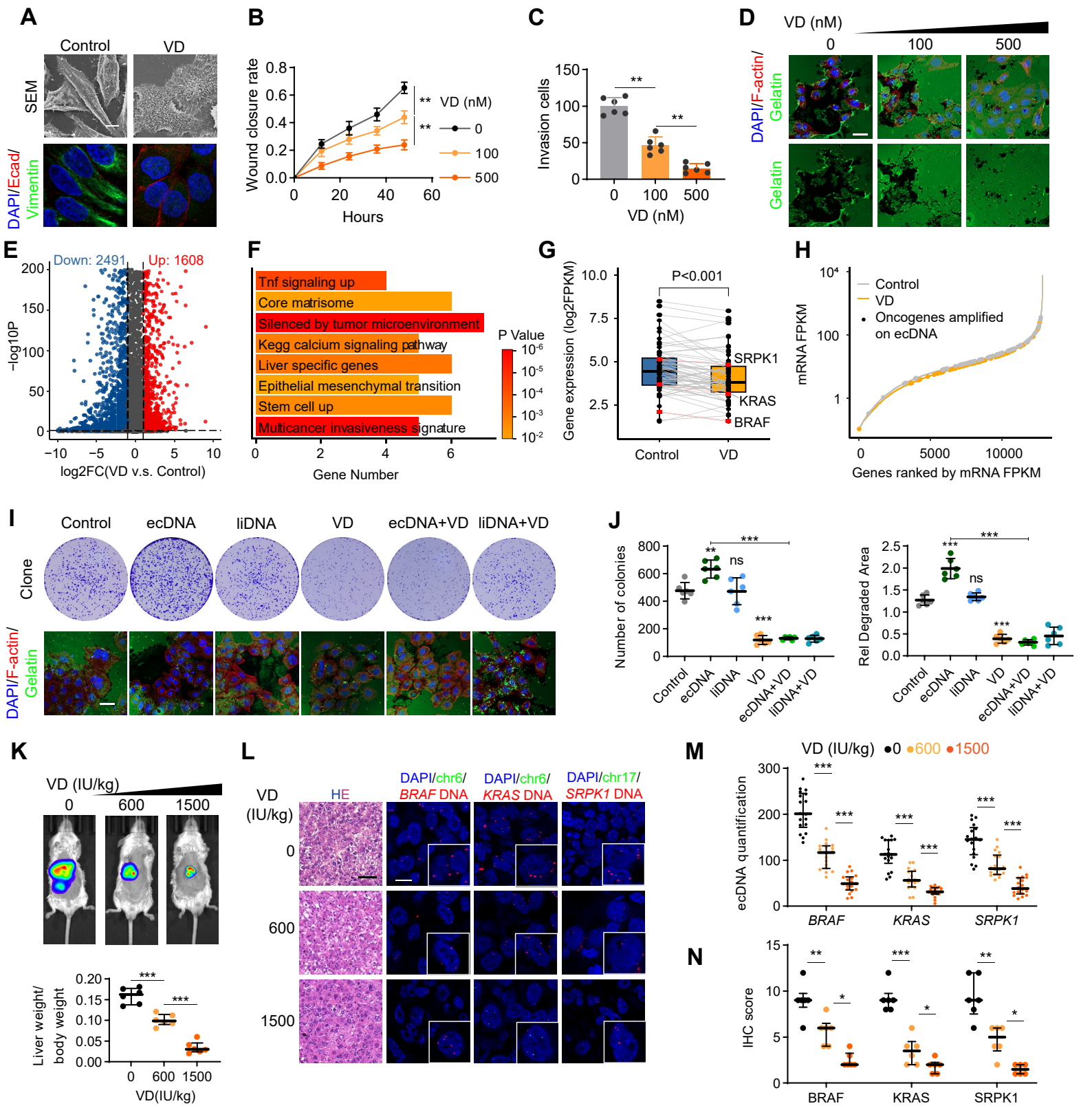
A
Control
VD
SEM
DAPI/Ecad/
Vimentin
B
Wound closure rate
Hours
VD (nM)
0
100
500
C
Invasion cells
VD (nM)
D
VD (nM)
0
100
500
DAPI/F-actin/
Gelatin
Gelatin
E
Down: 2491
Up: 1608
−log10P
log2FC(VD v.s. Control)
F
Tnf signaling up
Core matrisome
Silenced by tumor microenvironment
Kegg calcium signaling pathway
Liver specific genes
Epithelial mesenchymal transition
Stem cell up
Multicancer invasiveness signature
P Value
Gene Number
G
P<0.001
Gene expression (log2FPKM)
SRPK1
KRAS
BRAF
Control
VD
H
Control
VD
Oncogenes amplified
on ecDNA
mRNA FPKM
Genes ranked by mRNA FPKM
I
Control
ecDNA
liDNA
VD
ecDNA+VD
liDNA+VD
Clone
DAPI/F-actin/
Gelatin
J
Number of colonies
Rel Degraded Area
ns
K
VD (IU/kg)
0
600
1500
Liver weight/
body weight
VD(IU/kg)
L
VD
(IU/kg)
HE
DAPI/chr6/
BRAF DNA
DAPI/chr6/
KRAS DNA
DAPI/chr17/
SRPK1 DNA
M
VD (IU/kg)
ecDNA quantification
BRAF
KRAS
SRPK1
N
IHC score
BRAF
KRAS
SRPK1

Fig. 2. VD inhibits the malignant progression of HCC through ecDNA. (A) The morphologic detect with scanning electron microscopy (SEM) and Immunostaining of E-cadherin and vimentin signal in PLC-PRF-5 cells treated with DMSO or 25OHD (500 nM) for 48 h. Scale bar, 10 μm. **(B)** Quantification of wound closure rate in wound healing assay of PLC-PRF-5 cells treated with DMSO or 25OHD (100 nM or 500 nM) for 48 h. *n*=3, biological replicates. Statistics were calculated on biological replicates with two-tailed unpaired *t*-tests, $^{**}P < 0.01$. Error bars show mean with SD. **(C)** Quantification of invasion cells in transwell assay of PLC-PRF-5 cells treated with DMSO or 25OHD (100 nM or 500 nM) for 48 h. *n*=6, biological replicates. Statistics were calculated on biological replicates with two-tailed unpaired *t*-tests, $^{**}P < 0.01$. Error bars show mean with SD. **(D)** Fluorescent gelatin degradation and phalloidin/DAPI staining of PLC-PRF-5 cells treated with DMSO or 25OHD (100 nM or 500 nM) for 48 h. Scale bar, 40 μm. **(E)** Volcano plot showing up- and down-regulation of mRNA after 25OHD (500 nM, 48 h) treatment. **(F)** Gene annotation of 25OHD (500 nM, 48 h) downregulated mRNA. **(G)** B-allele frequency of all VD down regulated ecDNAs detected from Circle-seq involving genes using RNA-seq in Control group (DMSO, 48 h, blue) compared to the VD (25OHD, 500 nM, 48 h, orange) group. **(H)** ecDNA gene expression within the transcriptome of PLC-PRF-5 cells. The dots denote genes on ecDNA (circular amplification). **(I)** Representative images of colony formation (top) and fluorescent gelatin degradation and phalloidin/DAPI staining (bottom) of PLC-PRF-5 cells with indicated treatments. Control: treated with DMSO, ecDNA: transfection of purified ecDNA, liDNA: transfection of linearizing ecDNA. VD: treated with 500 nM 25OHD, ecDNA+VD: transfection of purified ecDNA and treated with 500 nM 25OHD, liDNA +VD: transfection of linearizing ecDNA and treated with 500 nM 25OHD. For the colony formation assay, the treatments time was 10 days. For fluorescent gelatin degradation assay, the treatments time was 48 h. Scale bar, 40 μm. **(J)** Quantification of the number of colonies (left) and relative degraded area (right) in PLC-PRF-5 cells. *n*=6, biological replicates. Statistics were calculated on biological replicates with two-tailed unpaired *t*-tests, $^{**}P < 0.01$, $^{***}P < 0.001$, ns, not significant. Error bars show mean with SD. **(K)** Representative in vivo images (top) of H22-luc-tumor-bearing-BALB/c mice with treatments of Ethanol or VD3 (600 IU/kg or 1500 IU/kg) for 2 months, and liver weight/body weight ratio was quantified (bottom). *n*=6, biological replicates. Statistics were calculated on biological replicates with two-tailed unpaired *t*-tests, $^{***}P < 0.001$. Error bars show median, upper and lower quartiles. **(L and M)** Representative image of HE staining and DNA FISH for liver tissues in H22-luc-tumor-bearing-BALB/c mice (**L**) and quantification of FISH signal by ecSeg

(**M**). Scale bar, 10 μm. Average fluorescence intensity in the nucleus in 18 cells of FISH images from 6 biologically independent samples were measured. Statistics were calculated on biological replicates with two-tailed unpaired *t*-tests, ***$P < 0.001$. Error bars show median, upper and lower quartiles. **(N)** Quantification of Immunohistochemical staining of BRAF, KRAS, SRPK1 in liver tissues of H22-luc-tumor-bearing-BALB/c mice. n=6, biological replicates. Statistics were calculated on biological replicates with unpaired *t*-test with Welch's correction, *$P < 0.05$, **$P < 0.01$, ***$P < 0.001$. Error bars show median, upper and lower quartiles.

A

Predicted Target Uniprot ID	Gene Name	SEA Z-Score	Swiss Probability	HITPICK Precision %
P11473	VDR	385.6534	0.8501666	100
P02774	GC	117.3356	0.2059157	100
P30304	CDC25A	83.2175	0.9247467	-
P23415	GLRA1	18.1304	0.8501666	-
Q13133	NR1H3	14.4565	0.1157367	-
Q12772	SREBF2	9.6585	0.1157367	-

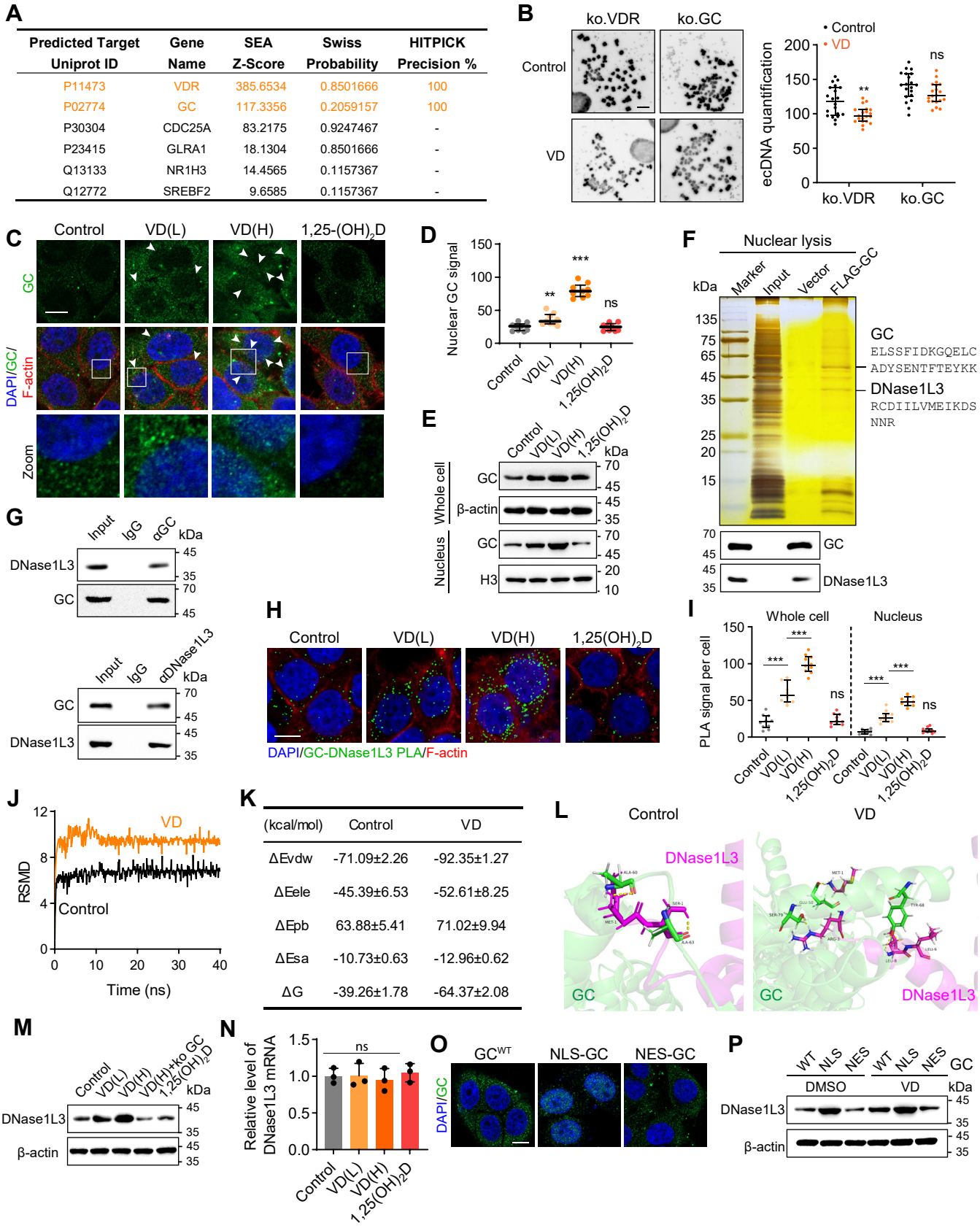

Fig. 3. VD promotes GC nucleation to interact with DNase1L3 and stabilizes its protein levels. **(A)** Prediction of VD targets through SEA, Swiss, and HITPICK. **(B)** Representative image (left) and quantification by ecSeg (right) of metaphase ecDNA in PLC-PRF-5 cells knocking out of VDR or GC and treated with DMSO or 25OHD (500 nM) for 48 h. Scale bar, 10 µm. 20 metaphase spreads from 3 biologically independent samples were counted. Statistics were calculated on biological replicates with unpaired *t*-test with Welch's correction. ***$P < 0.001$, ns, not significant. Error bars show median, upper and lower quartiles. **(C and D)** Immunostaining of GC signal (**C**) and quantification (**D**) of nuclear GC signal in PLC-PRF-5 cells treated with DMSO or 25OHD (500 nM) for 48 h. Scale bar, 10 µm. n=10, biological replicates. Statistics were calculated on biological replicates with two-tailed unpaired *t*-tests. **$P < 0.01$, ***$P < 0.001$; ns, not significant. Error bars show median, upper and lower quartiles. **(E)** Western blot analysis of GC expression level in the whole cell lysis and nucleus lysis of PLC-PRF-5 cells treated with DMSO, VD(L) (100 nM), VD(H) (500 nM) or 1,25$(OH)_2$D (500 nM) for 48 h. **(F)** Silver staining (top) of proteins acquired by FLAG-GC pull-down in nuclear lysis from PLC-PRF-5 cells treated with 25OHD (500 nM) for 48 h and western blot analysis (bottom) of GC and DNase1L3. **(G)** Co-immunoprecipitation assays in PLC-PRF-5 cells treated with 25OHD (500 nM) for 48 h with anti-GC followed by immunoblotting (IB) with antibodies against DNase1L3 and GC or with anti-DNase1L3 followed by IB with anti-GC and DNase1L3. **(H and I)** PLA assays with GC and DNase1L3 in PLC-PRF-5 cells treated with DMSO, VD(L) (100 nM), VD(H) (500 nM) or 1,25$(OH)_2$D (500 nM) for 48 h (**H**). Scale bar, 10 µm. Quantification of PLA signal in whole cell and nucleus were shown (**I**). n=10, biological replicates. Statistics were calculated on biological replicates with two-tailed unpaired *t*-tests. ***$P < 0.001$; ns, not significant. Error bars show median, upper and lower quartiles. **(J)** The Root Mean Square Deviation (RSMD) during the molecular dynamic simulation shows that the 25OHD (500 nM)-containing system has a more stable binding of the two proteins during the molecular dynamics simulation. **(K)** Changes in Van der Waals potential energy (ΔEvdw), electrostatic potential energy (ΔEele), polar interaction potential energy (ΔEpb), solvation potential energy (ΔEsa) and binding free energy (ΔG) during molecular dynamics simulation, showing that the binding of GC to DNase1L3 protein is more stable in the VD-containing system. **(L)** The stable structure of GC binding to DNase1L3 protein obtained by molecular dynamic simulation with or without VD. **(M)** Western blot analysis of DNase1L3 in ko GC PLC-PRF-5 cells with treatment of VD(H) (500 nM) for 48 h or wild type PLC-PRF-5 cells treated with DMSO, VD(L) (100 nM), VD(H) (500 nM) or 1,25$(OH)_2$D (500

nM) for 48 h. **(N)** The level of DNase1L3 mRNA was detected by RT-qPCR in PLC-PRF-5 cells treated with DMSO, VD(L) (100 nM), VD(H) (500 nM) or 1,25$(OH)_2$D (500 nM) for 48 h. *n*=3, biological replicates. Statistics were calculated on biological replicates with two-tailed unpaired *t*-tests. ns, not significant. Error bars show mean with SD. **(O)** Representative confocal images after transfection with GC^{WT}-EGFP, NLS-GC-EGFP or NES-GC-EGFP for 48 h. Scale bar, 10 µm. NLS: nuclear localization signals (MKRVLVLLLAVAFGHA). NES: nuclear export signals (MNLVDLQKKLEELELDEQQ). **(P)** Western blot analysis of DNase1L3 expression level in PLC-PRF-5 cells treated with DMSO or 25OHD (500 nM) and indicated transfection for 48 h. WT: transfection of empty vector, NLS: transfection of NLS-GC plasnid, NES: transfection of NES-GC plasnid.

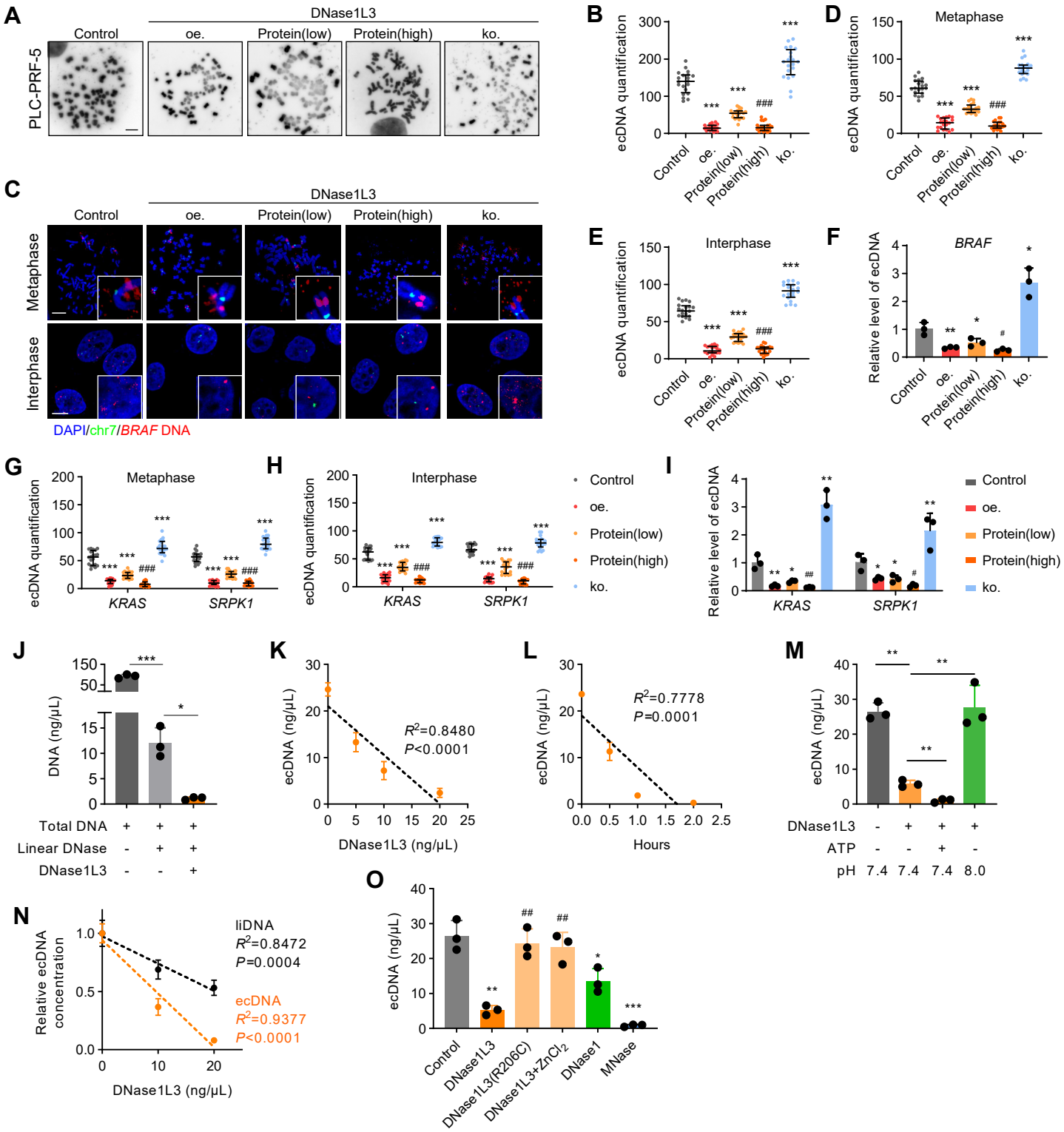
A
DNase1L3
Control
oe.
Protein(low)
Protein(high)
ko.
PLC-PRF-5
B
ecDNA quantification
Control
oe.
Protein(low)
Protein(high)
ko.
C
Metaphase
Interphase
DAPI/chr7/BRAF DNA
D
Metaphase
E
Interphase
F
BRAF
Relative level of ecDNA
G
Metaphase
KRAS
SRPK1
H
Interphase
I
J
DNA (ng/μL)
Total DNA
Linear DNase
DNase1L3
K
ecDNA (ng/μL)
DNase1L3 (ng/μL)
R2=0.8480
P<0.0001
L
R2=0.7778
P=0.0001
Hours
M
ATP
pH
N
Relative ecDNA concentration
liDNA
R2=0.8472
P=0.0004
ecDNA
R2=0.9377
P<0.0001
O
DNase1L3(R206C)
DNase1L3+ZnCl2
DNase1
MNase

Fig. 4. DNase1L3 degrades ecDNA in vitro and in vivo. (A and B) Representative images (**A**) and quantification (**B**) of metaphase ecDNA by ecSeg in PLC-PRF-5 cells after indicated treatment. Control: transfection of empty vector, oe: over expression of DNase1L3 plasmid, Protein(low): transfection of DNase1L3 protein (2 μg), Protein(high): transfection of DNase1L3 protein (10 μg), ko: transfection of DNase1L3 ko plasmid. Scale bar, 10 μm. 20 metaphase spreads from 3 biologically independent samples were counted. Statistics were calculated on biological replicates with unpaired *t*-test with Welch's correction. ***$P < 0.001$, compared with control unless otherwise indicated. #$P < 0.05$, compared with protein (low) unless otherwise indicated. Error bars show median, upper and lower quartiles. **(C to E)** Representative *BRAF* FISH images of metaphase ecDNA (top) and interphase ecDNA (bottom) signal in HCC cells after indicated treatments, Scale bar,10 μm (**C**). FISH signal quantification by ecSeg (**D and E**). 20 metaphase spreads or interphase cells of FISH images from 3 biologically independent samples were counted. Statistics were calculated on biological replicates with unpaired *t*-test with Welch's correction. ***$P < 0.001$, compared with control unless otherwise indicated. ###$P < 0.001$, compared with protein (low) unless otherwise indicated. Error bars show median, upper and lower quartiles. (**F**) QPCR detected of ecDNA levels of *BRAF* purified and isolated from PLC-PRF-5 cells with indicated treatments. *n*=3, biological replicates. Statistics were calculated on biological replicates with two-tailed unpaired t-tests, *$P < 0.05$, **$P < 0.01$, compared with control unless otherwise indicated. #$P < 0.05$, compared with protein (low) unless otherwise indicated. Error bars show mean with SD. **(G and H)** Quantification of FISH signal of *KRAS, SRPK1* in metaphase (**G**) and interphase (**H**) in PLC-PRF-5 cells with indicated treatments. 20 metaphase spreads or interphase cells of FISH images from 3 biologically independent samples were counted. Statistics were calculated on biological replicates with unpaired *t*-test with Welch's correction. ***$P < 0.001$, compared with control unless otherwise indicated. ###$P < 0.001$, compared with protein (low) unless otherwise indicated. Error bars show median, upper and lower quartiles. **(I)** QPCR detected of ecDNA levels of *SRPK1, KRAS* purified and isolated from PLC-PRF-5 cells with indicated treatments. *n*=3, biological replicates. Statistics were calculated on biological replicates with two-tailed unpaired t-tests. *$P < 0.05$, **$P < 0.01$, compared with control unless otherwise indicated. #$P < 0.01$, compared with protein (low) unless otherwise indicated. Error bars show mean with SD. **(J)** Quantification of ecDNA in PLC-PRF-5 cells after treated with plasmid-safe ATP-dependent DNase or co-incubation with DNase1L3 protein (10 ng/μL) at 37 °C for 1 h. *n*=3, biological replicates. Statistics were calculated on biological replicates with two-tailed unpaired t-tests.

*$P < 0.05$, ***$P < 0.001$. Error bars show mean with SD. **(K)** Quantification of purified ecDNA in PLC-PRF-5 cells after incubated with different concentrations of DNase1L3 protein (5 ng/μL, 10 ng/μL,20 ng/μL) at 37 °C for 1 h. *n*=3, biological replicates. Statistics were calculated on biological replicates with simple linear regression. Error bars show mean with SD. **(L)** Quantification of purified ecDNA in PLC-PRF-5 cells after incubated with DNase1L3 protein (10 ng/μl) at 37 °C of indicated time points (0.5 h, 1 h, 2 h). *n*=3, biological replicates. Statistics were calculated on biological replicates with simple linear regression. Error bars show mean with SD. **(M)** Quantification of purified ecDNA incubated with the indicated treatments at 37 °C for 1 h. DNase1L3 (10 ng/μL), ATP (the final concentration is 1 mM). *n*=3, biological replicates. Statistics were calculated on biological replicates with two-tailed unpaired t-tests. **$P < 0.01$. Error bars show mean with SD. **(N)** Quantification of ecDNA and linear DNA (liDNA) incubated with DNase1L3 protein (10 ng/μL, 20 ng/μL) at 37 °C for 1 h. *n*=3, biological replicates. Statistics were calculated on biological replicates with simple linear regression. Error bars show mean with SD. **(O)** Quantification of purified ecDNA incubated with the indicated treatments at 37 °C for 1 h. *n*=3, biological replicates. DNase1L3 (10 ng/μL), DNase1L3 (R206C) (10 ng/μL), DNase1 (5 μL), MNase (5 μL), $ZnCl_2$ (1 mM), the incubation was performed in a 60 μL reaction volume in the presence of 5 mM $MgCl_2$, 2.5 mM $CaCl_2$. Statistics were calculated on biological replicates with two-tailed unpaired t-tests. *$P < 0.05$, **$P < 0.01$, ***$P < 0.01$, compared with Control. ##$P<0.01$, compared with DNase1L3. Error bars show mean with SD.

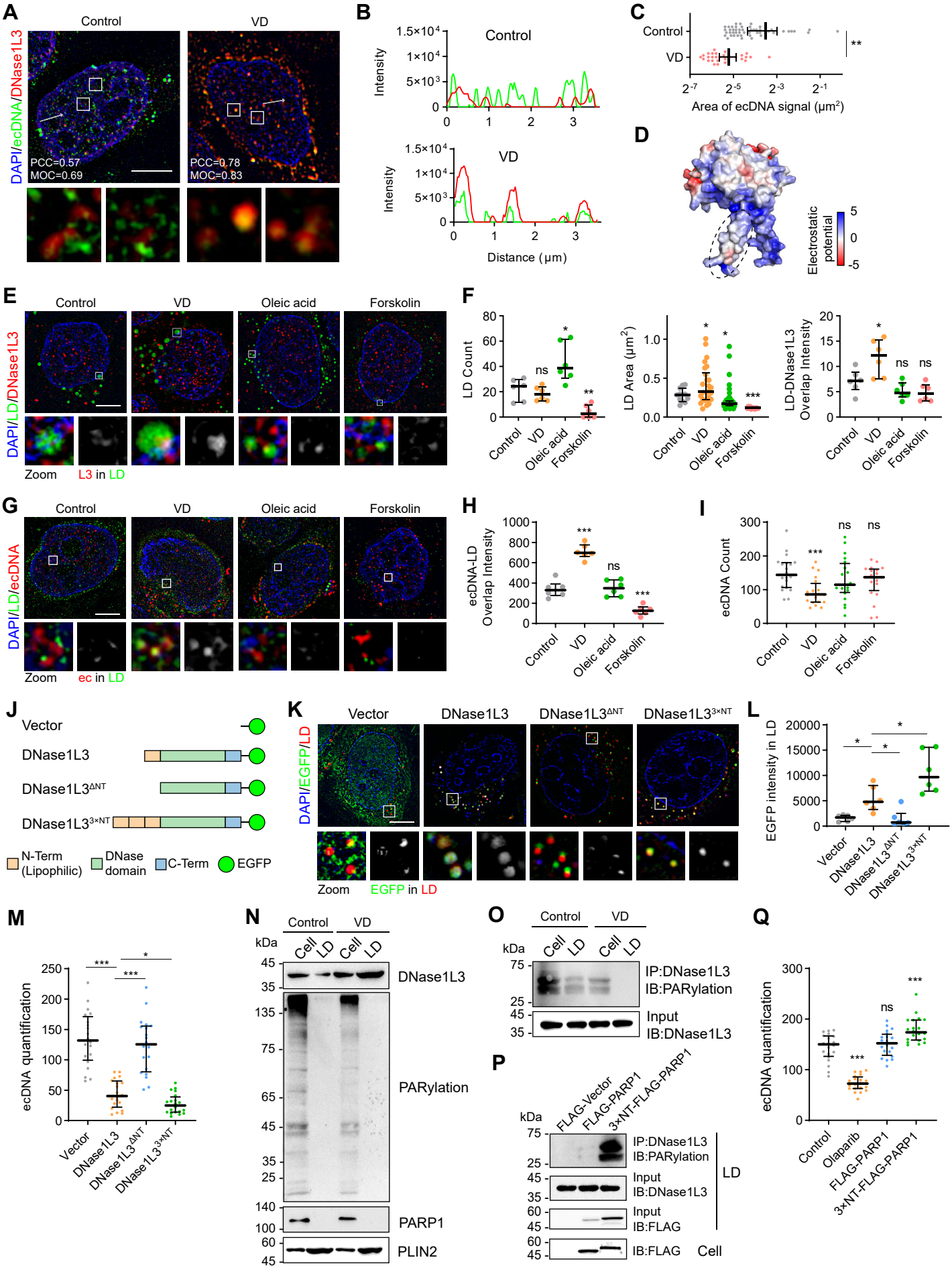
A
Control
VD
DAPI/ecDNA/DNase1L3
PCC=0.57
MOC=0.69
PCC=0.78
MOC=0.83
B
Control
VD
Intensity
Distance (μm)
C
Control
VD
Area of ecDNA signal (μm²)
D
Electrostatic potential
E
Control
VD
Oleic acid
Forskolin
DAPI/LD/DNase1L3
Zoom
L3 in LD
F
LD Count
LD Area (μm²)
LD-DNase1L3 Overlap Intensity
G
DAPI/LD/ecDNA
ec in LD
H
ecDNA-LD Overlap Intensity
I
ecDNA Count
J
Vector
DNase1L3
DNase1L3ΔNT
DNase1L3³ˣNT
N-Term (Lipophilic)
DNase domain
C-Term
EGFP
K
DAPI/EGFP/LD
EGFP in LD
L
EGFP intensity in LD
M
ecDNA quantification
N
kDa
Cell
LD
DNase1L3
PARylation
PARP1
PLIN2
O
IP:DNase1L3
IB:PARylation
Input
IB:DNase1L3
P
FLAG-Vector
FLAG-PARP1
3×NT-FLAG-PARP1
IB:FLAG
Q
Olaparib

Fig. 5. DNase1L3 affinitizes lipid droplets through lipophilic regions and degrades the ecDNA surrounded by lipid droplets. (A) Representative SIM images of ecDNA (indicated by *BRAF* DNA FISH, green) combined with Immunostaining of DNase1L3 signal (red) in PLC-PRF-5 cells treated with DMSO or 25OHD (500 nM) (top) for 48 h, corresponding zoom views of colocalization analysis were shown (bottom). PCC, Pearson's correlation coefficient; MOC, Mandas's overlap coefficient. Scale bar: 5 μm. **(B)** Quantification of the fluorescence intensity of FISH and DNase1L3 signals in PLC-PRF-5 cells treated with DMSO or 25OHD (500 nM) for 48 h. **(C)** Analysis of size of area of ecDNA signal in PLC-PRF-5 cells treated with DMSO or 25OHD (500 nM) for 48 h. At least 29 ecDNA signal from 3 biologically independent samples were counted. Statistics were calculated on biological replicates with unpaired *t* test with Welch's correction. $^{**}P < 0.01$. Error bars show mean with 95% CI. **(D)** Electrostatic potential of DNase1L3 molecular surface generated by APBS Electrostatics Plugin in Pymol software. The elliptical dotted line marks the lipophilic region. **(E)** Representative live-cell SIM images of EGFP-labelled DNase1L3 and BODIPY staining of lipid droplets (top) and corresponding zoom views of the overlap of DNase1L3 and lipid droplets (bottom) in PLC-PRF-5 cells after DMSO, 25OHD (500 nM), oleic acid (200 μM) or forskolin (10 μM) treatments for 48 h. Scale bar: 5 μm. **(F)** Statistics of lipid droplets and DNase1L3 signal in PLC-PRF-5 cells after indicated treatments. *n*=6, biological replicates. Statistics were calculated on biological replicates with two-tailed unpaired t-tests. $^{*}P < 0.05$, $^{**}P < 0.01$, $^{***}P < 0.001$, ns, not significant, compared with control unless otherwise indicated. Error bars show median, upper and lower quartiles. **(G)** Representative SIM images of *BRAF* DNA FISH and Bodipy staining of lipid droplets in PLC-PRF-5 cells after after DMSO, 25OHD (500 nM), oleic acid (200 μM) or forskolin (10 μM) treatments for 48 h. Scale bar: 5 μm. **(H and I)** Statistics of overlap of ecDNA and LD, *n*=6, biological replicates (**H**) and ecDNA FISH signal of 20 interphase FISH images in PLC-PRF-5 cells from 3 biologically independent samples were counted after indicated treatments(**I**). Statistics were calculated on biological replicates with unpaired *t* test with Welch's correction. $^{***}P < 0.001$, ns, not significant, compared with control. Error bars show median, upper and lower quartiles. **(J)** Schematic of the different DNase constructs used. **(K)** Representative live-cell SIM images of EGFP-labelled different DNase1L3 constructs and Bodipy staining of lipid droplets (top) and corresponding zoom views of the overlap images (bottom) in PLC-PRF-5 cells after transfection of indicated DNase1L3 constructs. Scale bar: 5 μm. **(L)** Quantification of the lipid droplets containing EGFP intensity in PLC-PRF-5 cells after transfection of indicated plasmids. *n*=6, biological replicates. Statistics were

calculated on biological replicates with unpaired *t* test with Welch's correction. $*P < 0.05$. Error bars show median, upper and lower quartiles. **(M)** Quantification of the number of ecDNA in PLC-PRF-5 cells after transfection of indicated plasmids. n=6, biological replicates. Statistics were calculated on biological replicates with unpaired *t* test with Welch's correction. $*P < 0.05$, $***P < 0.001$. Error bars show median, upper and lower quartiles. **(N)** Poly (ADP-ribosyl)ation (PARylation) of the whole cell proteins and LD binding protein in PLC-PRF-5 cells treated with DMSO or 25OHD (500 nM) for 48 h were monitored by immunoblot analysis with antibodies to PAR. PARP1, DNase1L3 and classical LD binding protein PLIN2 in the whole cell lysis and LD component were measured respectively. **(O)** Western blot analysis of PARylation of DNase1L3 in the whole cell lysis and LD component in PLC-PRF-5 cells treated with DMSO or 25OHD (500 nM) for 48 h. **(P)** Co-immunoprecipitation assays in LD component from PLC-PRF-5 cells after transfection of PARP1 or 3×NT-PARP1 overexpression plasmids with anti-DNase1L3 followed by immunoblotting with antibodies against PAR. **(Q)** Quantification of metaphase ecDNA by ecSeg in PLC-PRF-5 cells after transfection of Flag-PARP1, 3×NT-PARP1 or treated with PARP1 inhibitor Olaparib (20 μM) for 48 h. 20 metaphase spreads from 3 biologically independent samples were counted. Statistics were calculated on biological replicates with unpaired *t*-test with Welch's correction. $***P < 0.01$, ns, not significant, compared with control unless otherwise indicated. Error bars show median, upper and lower quartiles.

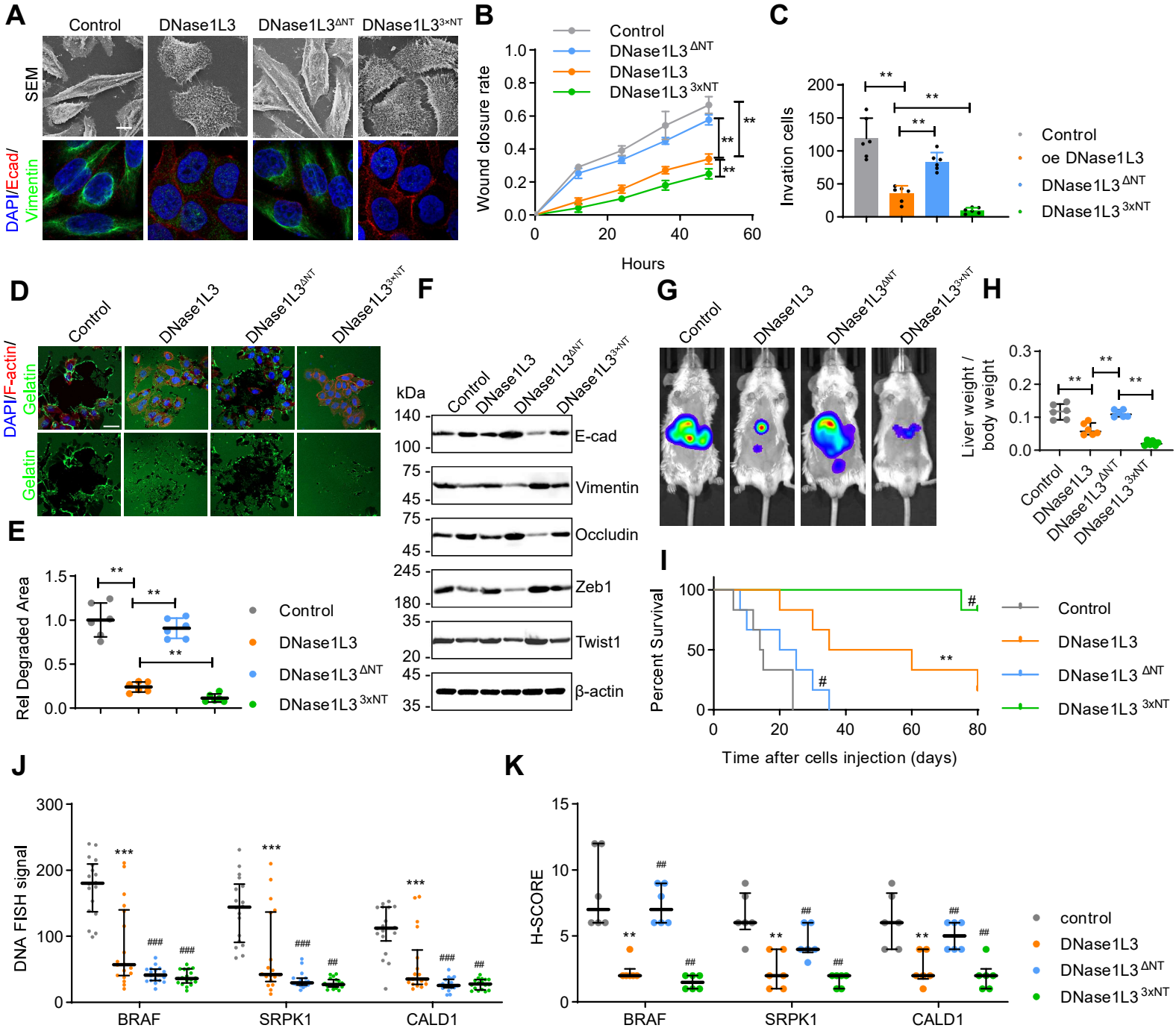
A
Control
DNase1L3
DNase1L3ΔNT
DNase1L3 3×NT
SEM
DAPI/Ecad/Vimentin
B
Control
DNase1L3 ΔNT
DNase1L3
DNase1L3 3xNT
Wound closure rate
Hours
C
Invation cells
Control
oe DNase1L3
DNase1L3 ΔNT
DNase1L3 3xNT
D
DAPI/F-actin/Gelatin
Gelatin
E
Rel Degraded Area
F
kDa
E-cad
Vimentin
Occludin
Zeb1
Twist1
β-actin
G
H
Liver weight / body weight
I
Percent Survival
Time after cells injection (days)
J
DNA FISH signal
BRAF
SRPK1
CALD1
K
H-SCORE
control
DNase1L3
DNase1L3 ΔNT
DNase1L3 3xNT

Fig. 6. DNase1L3 inhibits the malignant progression of HCC dependent on lipophilic regions. **(A)** The morphologic detect with scanning electron microscopy (top) and Immunostaining (bottom) of E-cadherin and vimentin signals in PLC-PRF-5 cells transfected with vector, DNase1L3 over expression plasmid, DNase1L3$^{\Delta NT}$ expression plasmid or DNase1L3 $^{3\times NT}$ expression plasmid for 48 h. Scale bar, 10 μm. **(B)** Quantification of wound closure rate in wound healing assay of PLC-PRF-5 cells treated as indicated. *n*=3, biological replicates. Statistics were calculated on biological replicates with two-tailed unpaired *t*-tests, $^{**}P < 0.01$. Error bars show mean with SD. **(C)** Quantification of invasion cells in transwell assay of PLC-PRF-5 cells treated as indicated. *n*=6, biological replicates. Statistics were calculated on biological replicates with two-tailed unpaired *t*-tests, $^{**}P < 0.01$. Error bars show mean with SD. **(D and E)** Fluorescent gelatin degradation and phalloidin/DAPI staining of PLC-PRF-5 cells treated as indicated (**D**) and quantification of degradation area (**E**). Scale bar, 40 μm. *n*=6, biological replicates. Statistics were calculated on biological replicates with two-tailed unpaired *t*-tests, $^{**}P < 0.01$. Error bars show mean with SD. **(F)** The levels of EMT related proteins were detected by western blot in PLC-PRF-5 cells treated as indicated. **(G and H)** Representative in vivo images (**G**) of H22-luc-tumor-bearing-BALB/c mice with indicated treatments and liver weight/body weight ratio was quantified (**H**). *n*=6, biological replicates. Statistics were calculated on biological replicates with two-tailed unpaired *t*-tests, $^{**}P < 0.01$. Error bars show median, upper and lower quartiles. **(I)** Kaplan–Meier curves showing percentage of survival of H22-luc-tumor-bearing-BALB/c mice after indicated treatments. *n*=6, biological replicates. Statistics were calculated on biological replicates with Kaplan–Meier analysis. $^{**}P < 0.01$, compared with control unless otherwise indicated; $^{\#}P < 0.05$, compared with DNase1L3. **(J)** Quantification of FISH for liver tissue in H22-luc-tumor-bearing-BALB/c mice with indicated treatments. Average fluorescence intensity in the nucleus in 18 cells of FISH images from 6 biologically independent samples were measured. Statistics were calculated on biological replicates with two-tailed unpaired *t*-tests, $^{***}P < 0.01$, compared with control; $^{\#\#}P < 0.01$, $^{\#\#\#}P < 0.001$, compared with DNase1L3. Error bars show median, upper and lower quartiles. **(K)** Quantification of pathological score of Immunohistochemical staining of BRAF, KRAS,SRPK1 in liver tissues of H22-luc-tumor-bearing-BALB/c mice. *n*=6, biological replicates. Statistics were calculated on biological replicates with two-tailed unpaired *t*-tests, $^{**}P < 0.01$, compared with control; $^{\#\#}P < 0.01$, compared with DNase1L3. Error bars show median, upper and lower quartiles.

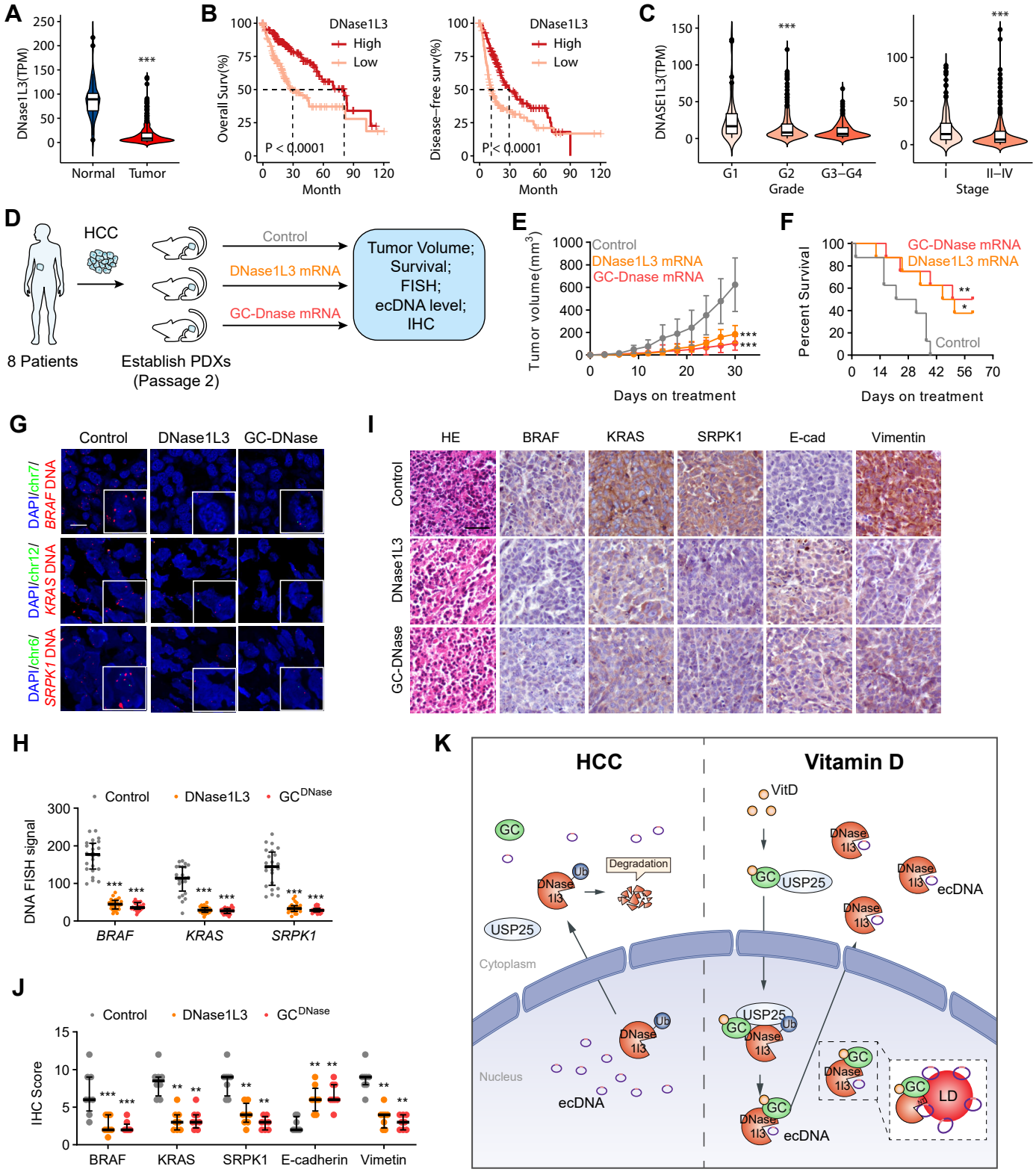
A
DNase1L3(TPM)
Normal
Tumor
B
Overall Surv(%)
DNase1L3
High
Low
P < 0.0001
Month
Disease−free surv(%)
P < 0.0001
C
DNASE1L3(TPM)
G1
G2
G3−G4
Grade
I
II−IV
Stage
D
HCC
8 Patients
Establish PDXs
(Passage 2)
Control
DNase1L3 mRNA
GC-Dnase mRNA
Tumor Volume;
Survival;
FISH;
ecDNA level;
IHC
E
Tumor volume(mm3)
Control
DNase1L3 mRNA
GC-Dnase mRNA
Days on treatment
F
Percent Survival
GC-DNase mRNA
DNase1L3 mRNA
Control
Days on treatment
G
Control
DNase1L3
GC-DNase
DAPI/chr7/BRAF DNA
DAPI/chr12/KRAS DNA
DAPI/chr6/SRPK1 DNA
I
HE
BRAF
KRAS
SRPK1
E-cad
Vimentin
Control
DNase1L3
GC-DNase
H
Control
DNase1L3
GCDNase
DNA FISH signal
BRAF
KRAS
SRPK1
J
Control
DNase1L3
GCDNase
IHC Score
BRAF
KRAS
SRPK1
E-cadherin
Vimetin
K
HCC
Vitamin D
VitD
GC
Degradation
Ub
DNase 1l3
USP25
Cytoplasm
Nucleus
ecDNA
LD

Fig. 7. DNase1L3-related mRNA drugs have the potential therapeutic effects on the clinical treatment of HCC. (A) mRNA expression level (TPM) of DNase1L3 in normal and tumor tissues of HCC in the TCGA dataset. **(B)** Kaplan–Meier curves showing percentage of the overall survival (left) and disease-free survival (right) of the higher and lower expression of DNase1L3 in the TCGA dataset. **(C)** DNase1L3 mRNA expression level (TPM) in different Grade (left) and Stage (right) in the TCGA dataset. One-way ANOVA and Tukey's multiple comparisons test was used. **(D)** Schematic of the experimental workflow of PDX. **(E)** Tumor growth of mice was measured starting 2 months after established of PDX mouse model with indicated mRNA treatments. n=8, biological replicates. Statistics were calculated on biological replicates with two-tailed unpaired t-tests, ***$P < 0.001$, compared with control unless otherwise indicated. Error bars show mean with SD. **(F)** Kaplan–Meier curves showing percentage of survival of mice after established of PDX mouse model with indicated mRNA treatments. n=8, biological replicates. Statistics were calculated on biological replicates with Kaplan–Meier analysis. *P<0.05, **$P < 0.01$, compared with control unless otherwise indicated. **(G and H)** Representative images of DNA FISH for tumors of PDX model after indicated treatments (**G**) and the FISH signals were quantified (**H**). Scale bar: 10 μm. Average fluorescence intensity in the nucleus in 24 cells of FISH images from 8 biologically independent samples were measured. Statistics were calculated on biological replicates with two-tailed unpaired t-tests, ***$P < 0.001$, compared with control. Error bars show median, upper and lower quartiles. **(I and J)** Representative images (**I**) of HE staining and Immunohistochemical staining of BRAF, KRAS, SRPK1, E-cadherin and vimentin for tumors of PDX mouse model and pathological scores were quantified (**J**). Scale bar: 40 μm. n=8, biological replicates. Statistics were calculated on biological replicates with two-tailed unpaired t-tests, **P<0.01, ***$P < 0.001$, compared with control. Error bars show median, upper and lower quartiles. **(K)** Proposed model for the role of VD, GC, DNase1L3 in HCC.